Relevant use of Klotho in FGF19 subfamily signaling system in vivo

Ken-ichi Tomiyama[a,b,1], Ryota Maeda[a,b,1], Itaru Urakawa[c], Yuji Yamazaki[c], Tomohiro Tanaka[a,b], Shinji Ito[a,b], Yoko Nabeshima[a,b], Tsutomu Tomita[d], Shinji Odori[d], Kiminori Hosoda[d], Kazuwa Nakao[d], Akihiro Imura[a,b], and Yo-ichi Nabeshima[a,b,2]

[a]Department of Pathology and Tumor Biology, Graduate School of Medicine, Kyoto University, Sakyo-Ku, Kyoto 606-8501, Japan; [c]Pharmaceutical Research Laboratories, Kyowa Hakko Kirin Company, Ltd., Takasaki, Gunma 370-1295, Japan; [b]Core Research for Evolutional Science and Technology, Japan Science and Technology Corporation, Kawaguchi-shi, Saitama 332-0012, Japan; and [d]Department of Medicine and Clinical Science, Graduate School of Medicine, Kyoto University, Sakyo-Ku, Kyoto 606-8501, Japan

Communicated by Yoshito Kaziro, Kyoto University, School of Medicine, Kyoto, Japan, December 9, 2009 (received for review September 28, 2009)

α-Klotho (α-Kl) and its homolog, β-Klotho (β-Kl) are key regulators of mineral homeostasis and bile acid/cholesterol metabolism, respectively. FGF15/ humanFGF19, FGF21, and FGF23, members of the FGF19 subfamily, are believed to act as circulating metabolic regulators. Analyses of functional interactions between α- and β-Kl and FGF19 factors in wild-type, *α-kl*$^{-/-}$, and *β-kl*$^{-/-}$ mice revealed a comprehensive regulatory scheme of mineral homeostasis involving the mutually regulated positive/negative feedback actions of α-Kl, FGF23, and 1,25(OH)$_2$D and an analogous regulatory network composed of β-Kl, FGF15/humanFGF19, and bile acids that regulate bile acid/cholesterol metabolism. Contrary to in vitro data, β-Kl is not essential for FGF21 signaling in adipose tissues in vivo, because (*i*) FGF21 signals are transduced in the absence of β-Kl, (*ii*) FGF21 could not be precipitated by β-Kl, and (*iii*) essential phenotypes in *Fgf21*$^{-/-}$ mice (decreased expressions of *Hsl* and *Atgl* in WAT) were not replicated in *β-kl*$^{-/-}$ mice. These findings suggest the existence of Klotho-independent FGF21 signaling pathway(s) where undefined cofactors are involved. One-to-one functional interactions such as α-Klotho/FGF23, β-Klotho/FGF15 (humanFGF19), and undefined cofactor/FGF21 would result in tissue-specific signal transduction of the FGF19 subfamily.

bile acid | cholesterol | mineral homeostasis | Cyp genes | energy source

The physiological roles of the Klotho family have remained puzzling since the original mutant mouse was developed (1). α-Kl deficiency in mice led to a characteristic phenotype resembling premature aging symptoms in human (1). Thereafter, we found that the overproduction of 1,25(OH)$_2$D and altered mineral-ion homeostasis are the major cause of these premature aging-like phenotypes observed in *α-kl*$^{-/-}$ mice, because the lowering of 1,25(OH)$_2$D activity by dietary restriction (a regimen in which *α-kl*$^{-/-}$ mice are fed a vitamin D–deficient diet) (2) is able to rescue the premature aging–like phenotypes and enable *α-kl*–deficient mice to survive normally without obvious abnormalities. Recently we have reported that α-Kl interacts with fibroblast growth factor 23 (FGF23) in kidney and plays an essential role in maintaining serum 1,25(OH)$_2$D levels by regulation of key active vitamin D–metabolizing enzymes, 1α-hydroxylase (Cyp27b1), and 24-hydroxylalse (Cyp24) (3). We also found that α-Kl binds to Na^+,K^+-ATPase in choroid plexus, parathyroid glands, and the distal convoluted tubules (DCT) of the kidney where extracellular calcium concentration is coordinately regulated (4). In these tissues, Na^+,K^+-ATPase activity is controlled in an α-Kl–dependent manner for transepithelial calcium transport in the choroid plexus and DCT, and for regulated PTH secretion in the parathyroid glands. By associating with both Na^+,K^+-ATPase and circulating FGF23, α-Kl plays a multifunctional role in α-Kl expressing tissues to regulate calcium and phosphate concentrations in vivo. This led to the concept that α-Kl is a regulator that integrates mineral homeostasis (5).

We next identified *β-kl*, which shares structural identity and characteristics with *α-kl* (6). β-Kl is predominantly expressed in the liver, pancreas, and adipose tissues (6) distinct from α-Kl expressing tissues (1, 2). To understand the biological role(s) of β-Kl, we generated a mouse line lacking *β-kl* (7). Although there were no gross abnormalities in the appearance of *β-kl*$^{-/-}$ mice, these mice exhibited an altered metabolism of bile acids, a group of structurally diverse molecules that are primarily synthesized in the liver from cholesterol, promote absorption of dietary lipids in the intestine, and stimulate biliary excretion of cholesterol (8). The enterohepatic circulation of bile acids is regulated largely in hepatocytes where bile acid biosynthesis is regulated by rate-limiting enzymes; cholesterol 7α-hydroxylase (Cyp7a1) and sterol 12α-hydroxylase (Cyp8b1) (8). Bile acids and oxysterols act as ligands to nuclear receptors regulating the expression of important genes in cholesterol homeostasis (9). Particularly, bile acids bind to the promoter region of the farnesoid X receptor (FXR), which induces transcription of small heterodimer partner (SHP), a negative regulator of Cyp7a1 and Cyp8b1, resulting in suppression of bile acids synthesis in a negative feedback manner (9).

Simultaneously, Inagaki et al. reported that FGF15 dramatically suppresses expression of Cyp7a1 through a gut–liver signaling pathway that is different from the FXR/SHP-mediated negative feedback system (10). Moreover, the association of bile acids with FXR leads to the increase of *Fgf15* expression in intestine, resulting in repression of Cyp7a1 in the liver. Importantly, this negative feedback effect was not observed in *Fgf15*$^{-/-}$ and *Fgfr4*$^{-/-}$ mice, and highlighted a concept that the binding of FGF15 with FGFR4 is involved in a second negative feedback system in bile acid metabolism. Taken together, analogous to the role of α-Kl in FGF23/FGFR1-mediated signal transduction, it was hypothesized that β-Kl plays a critical role in FGF15/FGFR4 mediated negative feedback regulation of *Cyp7a1* and *Cyp8b1* expression in the liver (11).

The mammalian FGF family currently consists of 22 members subdivided into seven subfamilies based on their structural similarity and modes of action (12). Most FGFs play an important role as paracrine factors regulating cell growth, regeneration, differentiation, and morphogenesis (13). However, it has been established that members of the FGF-19 subfamily, which also includes FGF21 and FGF23, differ in two important aspects from other FGF proteins. First, they have no or very small mitotic

Author contributions: Y.-i.N. designed research; K.-i.T., R.M., I.U., Y.Y., T. Tanaka, S.I., Y.N., and S.O. performed research; T. Tomita, K.H., K.N., and A.I. analyzed data; and A.I. and Y.-i.N. wrote the paper.

The authors declare no conflict of interest.

Freely available online through the PNAS open access option.

[1]K.-i.T. and R.M. contributed equally to this work.

[2]To whom correspondence should be addressed. E-mail: nabemr@lmls.med.kyoto-u.ac.jp.

This article contains supporting information online at www.pnas.org/cgi/content/full/0913986107/DCSupplemental.

www.pnas.org/cgi/doi/10.1073/pnas.0913986107

effects; and second, they exert their action via systemic, hormone-like effects as metabolic regulators. In fact, human FGF19 (hFGF19) and its murine ortholog FGF15, as well as FGF23, are secreted from ileal enterocytes and bone, respectively, and then circulate in the bloodstream to target tissues (12–14). The third member, FGF21 is predominantly synthesized in the liver (15) and has beneficial effects on several metabolic parameters in different animal models of obesity; recently, FGF21 has been postulated to be a newly found regulator of glucose metabolism through induction of glucose transporter 1 (GLUT 1) (16).

As first shown for FGF23 and subsequently for FGF19, FGF21 has been predicted to require a specific cofactor for its binding to a certain type of FGFR and subsequent activation of FGF21/FGFR signaling pathway. β-Kl has been reported as a candidate cofactor essential for bioactivity of FGF21 in in vitro studies (16–22). However, these have not been confirmed in in vivo studies. It is particularly important to examine (*i*) whether FGF21 signal transduction is abolished in *β-kl*$^{-/-}$ mice and (*ii*) whether the phenotypes of *β-kl*$^{-/-}$ mice significantly overlap with those of *Fgf21*-deficient mice (*Fgf21*$^{-/-}$) (23, 24).

Recent advances in understanding the signaling of FGF19 subfamilies have mainly been based on conventional in vitro experiments (13, 17, 19, 22), whereas in vivo verification of the association of FGF ligands and FGF receptor or of FGF ligands and Klotho family proteins, as well as the signal transduction (phosphorylation) cascades triggered by FGF 19 subfamilies have yet to be confirmed.

In the present study, we demonstrate the first manifest evidence revealing that whereas α-Kl and β-Kl are required for FGF23 and FGF15/hFGF19-mediated signaling pathways in vivo, respectively, β-Kl appears not to be essential for FGF21-mediated signal transduction in vivo.

Results

α-Kl–Dependent Vitamin D Regulation by FGF23. FGF23 is derived from bone and is essential for maintaining phosphate homeostasis and regulation of vitamin D metabolism. In WT mice, administration of hFGF23 results in remarkable suppression of serum 1,25-dihydroxyvitamin D [1,25$(OH)_2$D] through the repression of *Cyp27b1* and induction of *Cyp24* in the kidney. As we previously reported, serum concentrations of 1,25$(OH)_2$D in both *α-kl*$^{-/-}$ and *Fgf23*$^{-/-}$ mice were remarkably higher than that of WT mice (2, 25). Intriguingly, serum FGF23 in *α-kl*$^{-/-}$ mice was >8,000-fold that of WT mice (Fig. 1*A*). To analyze how α-Kl and FGF23 coordinately regulate vitamin D metabolism in the kidney, we analyzed the interactive actions of FGF23 and α-Kl in vivo. The FGFs used in these experiments (hFGF23, hFGF19, hFGF21) were prepared from CHO cell culture media, and their activities were estimated by measuring *Egr-1*-promotor directed Luciferase activities using Peak rapid cells with or without exogenous expression of *α-kl* or *β-kl* (Fig. S1). Furthermore the activity of hFGF21 was confirmed by up-regulation of *Glut1* mRNA in 3T3-L1 adipocyte. To minimize the effects of hypervitaminosis D, a major cause of the abnormalities observed in *α-kl*$^{-/-}$ mice, we used *α-kl*$^{-/-}$ mice fed with a vitamin D–deficient diet, in which serum 1,25$(OH)_2$D levels were normal and consequently most of the premature aging–like phenotypes were alleviated (2).

hFGF23 administration induced a significant decrease in serum 1,25$(OH)_2$D levels in WT mice, whereas no effect was observed in *α-kl*$^{-/-}$ mice (Fig. 1*B*). Consistently, in WT kidneys injected with hFGF23, *Cyp27b1* expression was reduced >13-fold, whereas *Cyp24* expression was induced >5-fold (Fig. 1 *C* and *D*). However, no significant effect of hFGF23 was found on the expression of *Cyp27b1* and *Cyp24* in *α-kl*$^{-/-}$ mice. These results offer direct evidence that α-Kl is essential for FGF23-derived repression of *Cyp27b1* and induction of *Cyp24* in vivo. In addition, we found that the administration of hFGF23 resulted in down-regulation of α-Kl expression (Fig. 1*E*), probably because α-Kl is a target of FGF23 signal transduction and/or because of a secondary effect of decreased 1,25$(OH)_2$D, an inducer of α-Kl gene expression (2). These data implicate an elaborate mutual negative feedback system composed of α-Kl, FGF23, and 1,25$(OH)_2$D in mineral-ion maintenance (Fig. 5*A*).

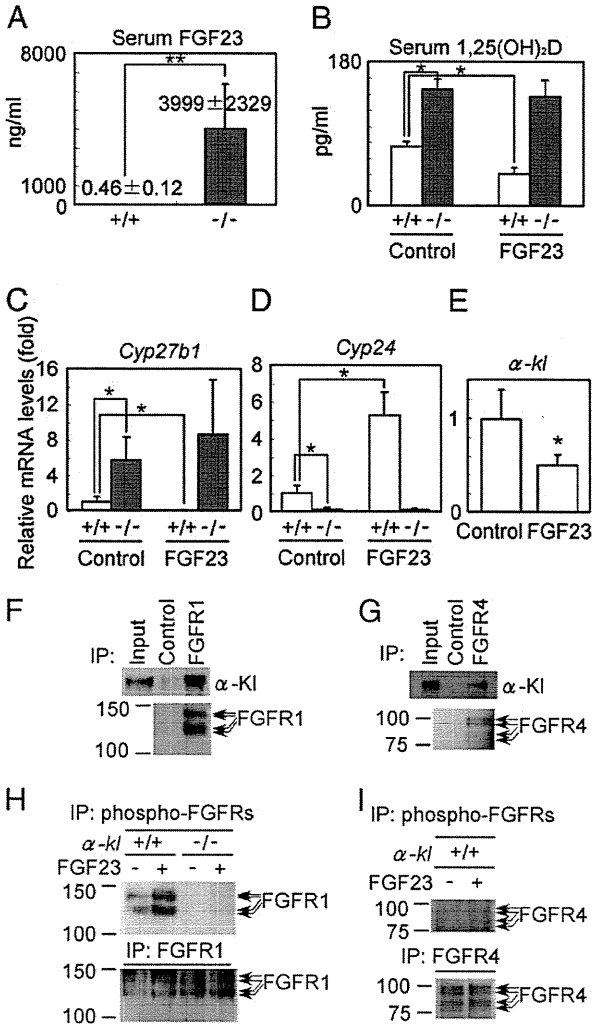

Fig. 1. FGF23 is dependent on α-Kl for regulation of vitamin D synthesis in kidney (*A–E*). (*A*) Serum concentrations of FGF23 in WT and *α-kl*$^{-/-}$ were measured by ELISA. WT (*open bars*) and *α-kl*$^{-/-}$ (*filled bars*) mice (n = 4/group) were injected with recombinant hFGF23 (0.2 mg/kg) or PBS control. Mice were killed 4 h after injection, and serum concentrations of 1,25$(OH)_2$D (*B*) were measured. *Cyp27b1* (*C*), *Cyp24* (*D*), and *α-kl* (*E*) mRNA levels in kidney were analyzed by RT–quantitative PCR. In this and all other figures, error bars represent mean ± SD and are plotted as fold change. Data were derived from 8- to 10-week-old male mice on vitamin D–deficient diets. *P < 0.05; **P < 0.01. FGFR1 binds to α-Kl and is phosphorylated by FGF23 in the kidney (*F–I*). (*F*) Kidney lysates were precipitated with anti-FGFR1 antibody or with control IgG. Input is 0.01% of the kidney whole extract used for the immunoprecipitation. (*G*) Kidney lysates were precipitated with anti-FGFR4 antibody or with control IgG. Input is 0.2% of the kidney whole extract used for the immunoprecipitation. (*H*) The kidney lysates of WT and *α-kl*$^{-/-}$ mice were immunoprecipitated with the anti-phospho-FGFRs or the anti-FGFR1 antibody. The immunoprecipitates were separated by SDS/PAGE and blotted with anti-FGFR1 antibody. (*I*) Kidney lysates of WT mice were immunoprecipitated with the anti–phospho-FGFRs or the anti-FGFR4 antibody and then blotted with anti-FGFR4 antibody.

α-Kl–Dependent FGFR1 Phosphorylation by FGF23 in Vivo. Generally FGFs can bind to and activate cell surface tyrosine kinase FGF receptors and transduce signals to downstream molecules including MAP kinase (26). The FGF receptor family consists of

four members, FGFR1–4. With the exception of FGFR4, splicing variants in the third Ig-like domain (IIIb and IIIc types) have been identified for each member (12, 26). Recently, it has been reported that α-Kl binds to FGFRs in cultured cells (19) and converts the canonical FGFR1(III)c to a receptor specific for FGF23 (3). We therefore tested whether the above observations were valid in vivo. We first examined the interactions between α-Kl and FGFR1, and α-Kl and FGFR4 in the kidney. As observed in in vitro experiments, α-Kl was coprecipitated not only with FGFR1 but also with FGFR4 in the kidney (Fig. 1*F* and *G*). We then investigated whether these two receptors are activated by hFGF23 in the kidney (procedures are as in *SI Text* and Fig. S2). In WT mice, FGFR1 was activated in the kidney 10 min after injection of hFGF23 (Fig. 1*H*). In contrast, phosphorylation of FGFR4 was not detectable even after the injection of hFGF23 (Fig. 1*I*), suggesting that FGFR4 is not a major receptor responsible for FGF23 signaling in the kidney. As expected, we could not detect phosphorylation of FGFR1 in the kidney of α-$kl^{-/-}$ mice even after hFGF23 injection (Fig. 1*H*). In summary, we concluded that FGFR1 is preferentially activated by FGF23 in a α-Kl–dependent manner in the kidney.

β-Kl–Dependent Bile Acid Regulation by FGF15. Because the unusually elevated expression of Cyp7a1 was observed not only in β-$kl^{-/-}$ mice (7) but also in $Fgf15^{-/-}$ and $Fgfr4^{-/-}$ mice (10, 27), we predicted that β-Kl was involved in FGF15/FGFR4-signaling system. Based on studies in cultured cells, it was recently proposed that β-Kl is necessary for FGF15/hFGF19-mediated signal transduction in the liver (18, 22). To confirm this hypothesis in vivo, we first measured the mRNA levels of *Fgf15* in the terminal ileum of WT and β-$kl^{-/-}$ mice. Interestingly, *Fgf15* expression levels were ~12-fold increased in β-$kl^{-/-}$ mice compared with those of WT (Fig. 2*A*), analogous to the elevation of FGF23 expression in α-$kl^{-/-}$ mice (Fig. 1*A*). To evaluate the effect of FGF15 in vivo, we administered hFGF19 and analyzed *Cyp7a1* and *Cyp8b1* expression. In WT mice, the expression levels of *Cyp7a1* and *Cyp8b1* 6 h after hFGF19 injection resulted in >100-fold and >10-fold reductions, respectively (Fig. 2 *B* and *C*). These were comparable to findings in a previous study examining FGF15 (10), and thus we concluded hFGF19 could be used to evaluate bile acid regulation in mice. In contrast, the expression levels of *Cyp7a1* and *Cyp8b1* remained elevated in β-$kl^{-/-}$ livers even after the administration of hFGF19 (Fig. 2 *B* and *C*), demonstrating that β-Kl is essential for the negative regulation of Cyp7a1 and Cyp8b1 by FGF15/hFGF19 in vivo. β-Kl-regulated bile acid synthesis by FGF15/hFGF19 is further described in *SI* (Fig. S3).

β-Kl/FGFR4 Coexpression Is Required for FGF15 Signaling in Vivo. To monitor whether FGF15/hFGF19 signals are transduced in tissues other than the liver, we verified *Egr-1* (a zinc-finger transcription factor identified as an immediate-early gene induced by cellular stimulation) mRNA levels in β-Kl–expressing tissues (liver, adipose, pancreas, and salivary gland) as well as several β-Kl–nonexpressing tissues, since hFGF23 administration remarkably increased *Egr-1* expression and induced phosphorylation of 44/42 MAP kinase (ERK1/2) in the kidney where α-Kl is expressed (3). In WT liver, *Egr-1* expression level increased by >120-fold 30 min after hFGF19 administration compared with vehicle (Fig. 2*D*). With respect to other tissues, we observed a faint, but statistically significant *Egr-1* increase in pancreas (>5-fold) and in white adipose tissue (WAT) (~3-fold). Nonetheless, no remarkable changes were observed in other tissues including brown adipose tissue (BAT) and salivary gland despite β-Kl expression. As expected, in β-$kl^{-/-}$ mice injected with hFGF19, no significant induction of *Egr-1* was observed in any of the tissues evaluated (Fig. 2*D*), demonstrating that β-Kl is necessary but not sufficient for FGF15/hFGF19-mediated signal transduction. To address the question of why FGF15/hFGF19 signal is transduced in the liver, pancreas, and WAT, but not in BAT and salivary glands, we profiled the expression of various FGF receptors (FGFRs) in β-Kl–expressing tissues. As reported previously (10), FGFR4 is postulated to be the major receptor responsible for FGF15-mediated signal transduction in the liver. As for the pancreas and WAT, we did observe >2-fold and >6-fold lower *Fgfr4* expression compared with that in the liver, respectively. On the contrary, *Fgfr4* mRNA was not detected in the salivary glands and BAT (Fig. S4). Hence *Egr-1* up-regulation by hFGF19 could be observed in tissues where β-Kl and FGFR4 are coexpressed.

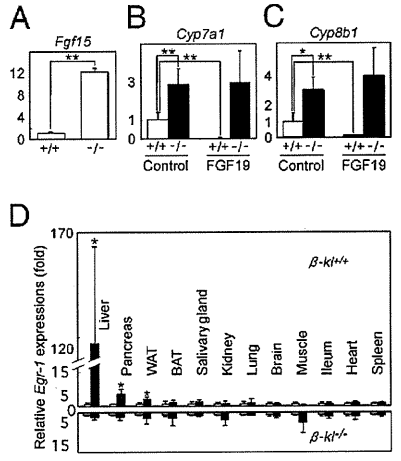

Fig. 2. FGF19 is dependent on β-Kl for regulation of bile acid synthesis in liver (*A–D*). (*A*) mRNA levels of *Fgf15* in terminal ileum in WT and β-$kl^{-/-}$ were measured by RTQ-PCR. WT mice (*open bars*) and β-$kl^{-/-}$ mice (*filled bars*) (n = 5/group) were injected with recombinant hFGF19 (1 mg/kg) or control medium. Mice were killed 6 h after injection and *Cyp7a1* (*B*) and *Cyp8b1* (*C*) mRNA levels in liver were measured by RT–quantitative PCR. Data were derived from 14- to 16-week-old male mice on standard diet. Egr-1 induction mediated by FGF19 in liver (*D*). hFGF19 (1 mg/kg) or control medium were injected into WT and β-$kl^{-/-}$ male mice (12–14 weeks old) on standard diet. Thirty minutes after injection, tissues in WT (*Upper*) and β-$kl^{-/-}$ (*Lower*) mice (n = 4/group) were excised. *Egr-1* mRNA levels were measured by RT-quantitative PCR. The expression levels of FGF19-injected mice (*filled bars*) and vehicle injected mice (*open bars*) are plotted as fold change. $*P < 0.05$; $**P < 0.01$.

To further demonstrate the contribution of β-Kl in the hepatic FGF15/hFGF19-mediated signaling cascade, we evaluated the phosphorylation of FGFR4 and downstream signaling molecules in vivo using the methods shown in Fig. 1 (Fig. S2 and *SI Text*). β-Kl could be efficiently precipitated by an anti-FGFR4 antibody (Fig. 3*A*) and the phosphorylation of FGFR4 was confirmed after hFGF19 treatment in WT liver (Fig. 3*B*). Unexpectedly, the amount of FGFR4 protein was significantly reduced in livers of β-$kl^{-/-}$ mice (Fig. 3*C*). To obtain an amount of FGFR4 equivalent to that obtained from WT mice, we concentrated the liver lysates from β-$kl^{-/-}$ mice and performed immunoprecipitation (Fig. S2 and *SI Text*). However, we could not detect enhanced activation of FGFR4 in β-$kl^{-/-}$ livers even after injection of hFGF19 (Fig. 3*D*). Consistent with a previous report (18), clear phosphorylation of ERK1/2 was observed in WT livers 10 min after hFGF19 injection, whereas it was undetectable in β-$kl^{-/-}$ livers (Fig. 3*E*), demonstrating that β-Kl is essential for the FGF15/hFGF19 directed activation of FGFR4 and downstream signaling cascade in the liver.

β-Kl Is Not Essential for FGF21-Mediated Signaling in Adipose Tissues. FGF21, a member of the FGF19 subfamily that is synthesized in the liver, has been reported to be a newly found regulator of glucose metabolism (16) and β-Kl has been postulated to be essential for its activity in in vitro studies (17, 20, 21). To examine the possible contribution of β-Kl in the FGF21 signaling system in vivo, we first administered recombinant hFGF21 to WT mice and analyzed *Egr-1* mRNA levels in multiple tissues (Fig. 4*A*). Before its use, we con-

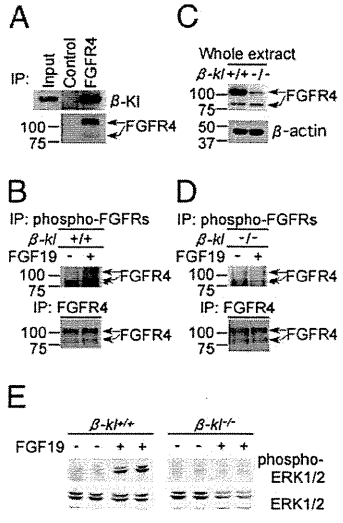

Fig. 3. FGFR4 binds to β-Kl and is phosphorylated by FGF19 in liver. (*A*) Liver lysates were precipitated with anti-FGFR4 antibody or with control IgG. Input is 1% of the liver whole extract used for the immunoprecipitation. The immunoprecipitates were separated by SDS/PAGE and blotted with anti-FGFR4 antibody. (*B, D,* and *E*) Ten minutes after injection of hFGF19 or control medium, livers were excised. Liver lysates from WT mice (*B*) and *β-kl*$^{-/-}$ mice (*D*) were immunoprecipitated with the anti–phospho-FGFRs or the polyclonal anti-FGFR4 antibody. Immunoprecipitates were blotted with anti-FGFR4 antibody. The arrowhead indicates a nonspecific band (Fig. S2). (*C*) Whole liver extracts of WT and *β-kl*$^{-/-}$ mice were blotted with anti-FGFR4 antibody or anti–β-actin antibody for a loading control. (*E*) Liver lysates from WT and *β-kl*$^{-/-}$ were immunoblotted with anti-phospho-ERK1/2 or anti-ERK1/2 antibodies (n = 2 in each case).

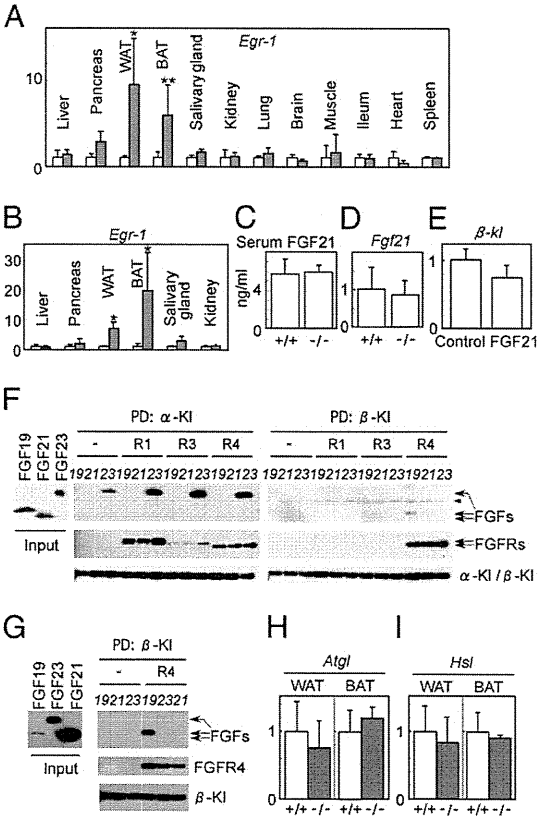

Fig. 4. β-Kl is not essential for FGF21-mediated signaling (*A–I*). Thirty minutes after injection, tissues in WT (n = 5/group) (*A*) and *β-kl*$^{-/-}$ mice (n = 4/group) (*B*) were excised. *Egr-1* mRNA levels were measured by RT-quantitative PCR. The expression levels of hFGF21 injected mice (*filled bars*) and vehicle injected mice (*open bars*) mice are plotted as fold change. Data were derived from 7- to 10-week-old male mice on standard diet. (*C*) Serum FGF21 concentrations of WT and *β-kl*$^{-/-}$ mice (n = 5–6/group) were measured by RIA. (*D*) *Fgf21* mRNA levels in livers of WT and *β-kl*$^{-/-}$ mice (n = 5–6/group) were measured by RT-quantitative PCR and are plotted as fold change. Data were derived from 15- to 20-week-old male mice on standard diet. hFGF21 (0.4 mg/kg) or control medium were injected into WT and *β-kl*$^{-/-}$ mice. (*E*) WT mice were injected with recombinant hFGF21 (0.4 mg/kg) or control medium (n = 5/group). Mice were killed 4 h after injection and *β-kl* mRNA levels in WAT were analyzed by RT-quantitative PCR. Data were derived from 10-week-old male mice on standard diet. (*F*) A 15-ng quantity of each FGF was pulled down (PD) by α-/β-Kl in the presence (R1, R3, or R4) or absence (–) of FGFRs. Input was 8% of samples used for the pull-down assay. Samples of pulled down by α-/β-Kl were analyzed by SDS/PAGE and blotted with antibodies (anti-His for FGFs, anti-Human Fc for FGFRs, and anti-GFP for α-/β-Kl). Arrowhead indicates a nonspecific band. (*G*) A 50-ng quantity of FGF19, 150 ng of FGF23, or 500 ng of FGF21 was precipitated by β-Kl in the presence or absence of FGFR4. Input was 1% of samples used for the assay. (*H* and *I*) *hsl* and *atgl* mRNA levels in WAT and BAT were analyzed by RT-quantitative PCR. Data were derived from 9- to 14-week-old female *β-kl*$^{+/+}$ and *β-kl*$^{-/-}$ mice (n = 5/group). *P < 0.05; **P < 0.01.

firmed the biological activity of the synthesized hFGF21. As shown in Fig. S5, our hFGF21 could enhance *Egr1*-derived luciferase reporter expression in a β-Kl–dependent manner at doses that were equivalent to those previously reported (17, 21). Moreover the hFGF21 up-regulated *Glut1* mRNA in 3T3-L1 adipocyte (Fig. S5) (16). Consistent with the in vitro results, in WT mice, *Egr-1* expression levels were significantly up-regulated by ~10-fold in WAT and >6-fold in BAT 30 min after injection of hFGF21 (Fig. 4*A* and Fig. S5). However, administration of hFGF21 also resulted in significant up-regulation of *Egr-1* mRNA levels in WAT and BAT from *β-kl*$^{-/-}$ mice (Fig. 4*B*). We next analyzed the serum levels of FGF21 and hepatic mRNA levels of *Fgf21* in WT and *β-kl*$^{-/-}$ mice. Unexpectedly, there was no significant genotype-dependent difference in mean serum protein concentrations of FGF21 nor hepatic *Fgf21* mRNA levels (Fig. 4 *C* and *D*). We also confirmed that *β-kl* expression was not affected by FGF21 administration (Fig. 4*E*). These results suggest that β-Kl is not essential for FGF21-mediated signaling in WAT and BAT. In addition, our prediction was further supported by the following experiments. First, to address the binding properties between β-Kl and FGF21, we performed pull-down assays using recombinant proteins. Although FGF19 was significantly bound by β-Kl in the presence of FGFR4, FGF21 could not be precipitated by β-Kl even with 10 fold amounts of FGF21 (Fig. 4 *F* and *G* and *SI Text*). Second, we compared the phenotypes of *Fgf21*$^{-/-}$ and *β-kl*$^{-/-}$ mice. Recently, Hotta et al. developed *Fgf21*$^{-/-}$ mice and reported that expression levels of hormone-sensitive lipase (*Hsl*) and adipose triglyceride lipase (*Atgl*) in WAT were decreased in *Fgf21*$^{-/-}$ mice to almost 50% compared with those of WT mice (23). The adipose phenotypes in *Fgf21*$^{-/-}$ mice may be an outcome of a deficiency in FGF21 signaling. Thus we analyzed the expression levels of these genes in the adipose tissues of *β-kl*$^{-/-}$ mice. Consequently, in both WAT and BAT, mRNA levels of *Hsl* and *Atgl* were not significantly altered between WT and *β-kl*$^{-/-}$ mice (Fig. 4 *H* and *I*). These data suggest that β-Kl may not necessarily be involved in the phenotypes observed in FGF21-deficient mice. Taken together, these results provide strong evidence that β-Kl is not essential for FGF21-mediated signaling in WAT and BAT. We therefore asked whether FGF21 signaling might require other unidentified components than β-Kl. We also analyzed *Glut1* mRNA levels 4 h after hFGF21 injection at concentrations that could induce *Egr-1* expression in WAT and BAT, but no apparent induction was observed, suggesting that *Glut1* is not a direct target of FGF21 signaling (28, 29).

Discussion

Various roles of Klotho family members have been reported (18, 22, 30); however, a consensus on the molecular functions of α-Kl

and β-Kl has not been reached. Based on these findings, we propose a comprehensive regulatory scheme of mineral homeostasis that is illustrated by the mutually regulated positive/negative feedback actions of α-Kl, FGF23, and $1,25(OH)_2D$ (Fig. 5*A*). In the present study, we found that FGF23 represses the expression of α-Kl and identified an essential role of α-Kl in FGF23-mediated phosphorylation of FGFR1 in the kidney. This leads to *Cyp27b1* down-regulation and *Cyp24* up-regulation, and results in inhibition of the synthesis of $1,25(OH)_2D$, an active form of vitamin D (3). $1,25(OH)_2D$ has prominent effects on the kidney, intestine, and bone. In the kidney, $1,25(OH)_2D$ activates vitamin D receptor (VDR) by binding to its ligand binding domain and negatively regulates the expression of *Cyp27b1* while positively regulating *Cyp24* and α-Kl expression (2). In the bone, $1,25(OH)_2D$ binds to VDR and induces FGF23 synthesis in osteocytes and osteoblasts (31) in hours/days. In turn, secreted FGF23 suppresses $1,25(OH)_2D$ synthesis and inorganic phosphate reabsorption in the kidney to adjust extracellular mineral concentrations. Collectively, α-Kl, in combination with FGF23, is involved in a signaling cascade that maintains extracellular calcium/phosphate levels within a narrow range.

The roles of β-Kl, FGF15, and FGFR4 in bile acid/cholesterol metabolism are schematically summarized in Fig. 5*B*. Consistent with a previous study (10, 22), i.v. injection of hFGF19 dramatically represses the expression of *Cyp7a1* and *Cyp8b1* and results in the inhibition of bile acid synthesis from cholesterol in WT livers. This suppression of *Cyp7a1* and *Cyp8b1* was not observed in *β-kl*$^{-/-}$ mice. Indeed, phosphorylation of FGFR4 and ERK1/2 was not detected in *β-kl*$^{-/-}$ livers even after hFGF19 administration. Our findings provide conclusive evidence proving the essential role of β-Kl in FGF15/hFGF19-mediated activation of FGFR4 and subsequent signal transduction that regulates bile acid synthesis. Particularly, by binding to FXR, bile acid induces SHP expression in the liver and FGF15 transcription in the terminal ileum. In turn, increased SHP and secreted FGF15 differentially suppress Cyp7a1/Cyp8b1 expression to down-regulate bile acid synthesis (8, 9, 11). In addition, we found mutual negative feedback regulations between β-Kl and FGF15, namely, a decrease in *β-kl* after hFGF19 administration and an increase in *Fgf15* in *β-kl* deficiency. In other words, *β-kl* ablation leads to impaired negative feedback regulation of bile acid metabolism, resulting in the overflow of bile acid pools. Consequently, in the *β-kl*$^{-/-}$ terminal ileum, chronic stimulation by elevated bile acid would lead to an unusual increase in *Fgf15* mRNA. We propose a scheme illustrating the bile acid/cholesterol homeostasis regulated by mutual negative/positive feedback actions of β-Kl, FGF15, and bile acids (Fig. 5*B*).

As shown in Fig. 5, the scheme for bile acid regulation by β-Kl/FGF15 is conceptually analogous to that of vitamin D metabolism, which involves α-Kl and FGF23. Both systems are regulated by the coordination of two types of feedback mechanisms mediated by end-metabolites, $1,25(OH)_2D$ or bile acids, that are in situ negative feedback regulation and target tissue mediated negative feedback loop. In the former pathway, the end-metabolite functions as a nuclear receptor ligand and negatively feeds back by repressing the expression of key regulatory enzymes (Cyp27b1 in the kidney or Cyp7a1/Cyp8b1 in the liver) in the relevant metabolic pathway responsible for the generation of end-metabolite itself. In the latter system, the end-metabolite is transported to the target tissue (bone or intestine) from a distal site and enhances the expression of FGF (FGF23 or FGF15) by binding to the nuclear receptor; VDR or FXR. Subsequently, secreted FGF acts as the regulator of a target tissue–mediated negative feedback loop in collaboration with α-Kl or β-Kl. The next question to be addressed is how these two pathways are coordinately involved in the rapid adjustment and long term maintenance of mineral homeostasis and bile acid metabolism.

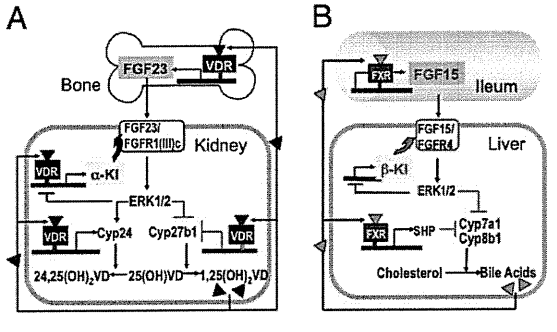

Fig. 5. Schematic representation of α-Kl/FGF23 and β-Kl/FGF15 systems. (*A*) Regulatory network of mineral homeostasis illustrated by the mutual positive/negative feedback actions of α-Kl, FGF23, and $1,25(OH)_2D$. (*B*) Regulatory network of bile acid/cholesterol metabolism represented by the mutual positive/negative feedback actions of β-Kl, FGF15, and bile acids.

In a previous report, we showed that i.v. injection of hFGF23 induces phosphorylation of ERK1/2 and specifically up-regulates the expression of *Egr-1* in the murine kidney (3). Here we demonstrate that α-Kl is required for FGF23 signal transduction in vivo. Likewise, i.v. injection of hFGF19 results in ERK1/2 phosphorylation and up-regulation of *Egr-1* in the liver in a β-Kl–dependent manner. Among β-Kl–expressing organs, significant up-regulation of *Egr-1* was observed in tissues where β-Kl and FGFR4 are coexpressed. Although induction of *Egr-1* in pancreas and WAT are slight, it occurs in a β-Kl–dependent manner. FGF15-mediated signal in pancreas and WAT could therefore be involved in bile acid homeostasis, but its functional importance has yet to be elucidated. Furthermore, the very high *Egr-1* induction in the liver strongly suggests that other elements, in addition to the coexpression of β-Kl and FGFR4, may endow this prominent hepatic signal activation. Recently, several groups have reported that α-Kl and β-Kl can bind to certain types of FGFRs. Those studies report preferences and differences for this binding that might be dependent on assay conditions. α-Kl solely binds to FGFR1(IIIc) in vitro (3), however α-Kl binds to not only FGFR1(IIIc) but also FGFR4 and weakly to FGFR3(IIIc) in cultured cells (30). Even though FGFR4 could precipitate α-Kl in the kidney, activation of FGFR4 by hFGF23 could not be detected. Further studies are required to understand how FGFR(s) is definitively and preferentially used for a particular FGF signal in vivo.

Serum levels of FGF23 and ileac *Fgf15* mRNA expression were intensively increased in *α-kl*$^{-/-}$ and *β-kl*$^{-/-}$ mice, respectively. Furthermore, administrations of hFGF23 and hFGF19 apparently suppressed the expression of *α-kl* and *β-kl*, respectively. In contrast, the serum levels of FGF21 and hepatic *Fgf21* mRNA expression were not increased in *β-kl*$^{-/-}$ mice, and *β-kl* expression was not significantly suppressed by hFGF21 in adipose. Consistent with a previous report that FGF21 induces ERK1/2 phosphorylation specifically in WAT (17), administration of FGF21 to WT mice significantly induced *Egr-1* mRNA expression in WAT and BAT, suggesting that WAT and BAT were the possible target tissues of FGF21. However, surprisingly, remarkable *Egr-1* inductions in WAT and BAT were also observed in *β-kl*$^{-/-}$ mice, indicating that β-Kl is not essential for FGF21 signal transduction in vivo. These in vivo results contrasted with those obtained from in vitro assays, as β-Kl is essential for FGF21-mediated signal transduction in vitro. We reproduced the direct binding of α-Kl and hFGF23 and also confirmed tricomplex formation of β-Kl, hFGF19, and FGFR4 but were unable to detect binding of α-/β-Kl and hFGF21 in our pull-down assay (Fig. 4*G*). Furthermore, we confirmed that the adipose phenotypes in *Fgf21*$^{-/-}$ mice did not overlap with those of *β-kl*$^{-/-}$ mice. This inconsistency leads to a postulation that β-Kl is not necessary for FGF21 signaling.

Currently, β-Kl is believed to be a common player essential for FGF15- and FGF21-mediated signal transduction. However, our present results, together with the data from Hotta et al. (23), do

not support this hypothesis. Possible explanations are that the response found in cultured cells might be caused by: (*i*) an artificial abundance of β-Kl and/or FGF21, (*ii*) peculiar characteristics of the cultured cells used in these experiments, and/or (*iii*) a combination of these two factors (17, 20, 21).

Recent studies have reported that FGF21 stimulates lipolysis in WAT and ketogenesis in the liver (32, 33). However, those results represent the pharmacological effects of sustained FGF21 treatment and thus include consequences that are secondary and indirectly induced by FGF21. We propose a β-Kl–independent response directly triggered by hFGF21 administration. Significant *Egr-1* upregulation in WAT and BAT are indicative that FGF21 mediates lipid metabolism in adipose tissues. The physiological target(s) of FGF21 signaling need to be clarified to understand how FGF21 functions as a regulator of lipid metabolism. Observations using genetic manipulation will lead us to a precise understanding of the roles of the FGF19 subfamily in metabolic homeostasis in vivo.

Materials and Methods

Measurement of Serum Parameters. Blood samples were collected from orbital cavities or hearts under anesthesia and were centrifuged to obtain sera. Serum FGF23 levels were measured by sandwich ELISA (Kainos Laboratory), which can quantify the intact form or FGF23 using human recombinant FGF23 as a standard. Serum $1,25(OH)_2D$ levels were analyzed by SRL, Inc. Serum FGF21 levels were measured by specific RIA (Phoenix Pharmaceuticals, Inc.).

Statistical Analysis. Unless otherwise noted, all values are expressed as mean ± SD. All data were analyzed by the Mann–Whitney *U* test. *P* values less than 0.05 were considered to be statistically significant.

More details are described in *SI Materials and Methods.*

ACKNOWLEDGMENTS. We thank Drs. M. Murata and R.Yu for critical reading of the manuscript and M. Terao and K. Yurugi for support in our experiments. This work was supported Ministry of Education, Science and Culture Grants 19045016 and 21390058 (to A.I.) and 17109004 (to Y-I.N.) and Ministry of Health and Welfare, and Labor Grant H16-genome-005 (to Y-I.N.).

1. Kuro-o M, et al. (1997) Mutation of the mouse Klotho gene leads to a syndrome resembling ageing. *Nature* 390:45–51.
2. Tsujikawa H, Kurotaki Y, Fujimori T, Fukuda K, Nabeshima Y (2003) Klotho, a gene related to a syndrome resembling human premature aging, functions in a negative regulatory circuit of vitamin D endocrine system. *Mol Endocrinol* 17:2393–2403.
3. Urakawa I, et al. (2006) Klotho converts canonical FGF receptor into a specific receptor for FGF23. *Nature* 444:770–774.
4. Imura A, et al. (2007) alpha-Klotho as a regulator of calcium homeostasis. *Science* 316: 1615–1618.
5. Nabeshima Y, Imura H (2008) alpha-Klotho: A regulator that integrates calcium homeostasis. *Am J Nephrol* 28:455–464.
6. Ito S, et al. (2000) Molecular cloning and expression analyses of mouse betaklotho, which encodes a novel Klotho family protein. *Mech Dev* 98:115–119.
7. Ito S, et al. (2005) Impaired negative feedback suppression of bile acid synthesis in mice lacking betaKlotho. *J Clin Invest* 115:2202–2208.
8. Russell DW (2003) The enzymes, regulation, and genetics of bile acid synthesis. *Annu Rev Biochem* 72:137–174.
9. Goodwin B, et al. (2000) A regulatory cascade of the nuclear receptors FXR, SHP-1, and LRH-1 represses bile acid biosynthesis. *Mol Cell* 6:517–526.
10. Inagaki T, et al. (2005) Fibroblast growth factor 15 functions as an enterohepatic signal to regulate bile acid homeostasis. *Cell Metab* 2:217–225.
11. Jones S (2008) Mini-review: Endocrine actions of fibroblast growth factor 19. *Mol Pharm* 5:42–48.
12. Itoh N, Ornitz DM (2004) Evolution of the Fgf and Fgfr gene families. *Trends Genet* 20:563–569.
13. Itoh N, Ornitz DM (2008) Functional evolutionary history of the mouse Fgf gene family. *Dev Dyn* 237:18–27.
14. Nishimura T, Utsunomiya Y, Hoshikawa M, Ohuchi H, Itoh N (1999) Structure and expression of a novel human FGF, FGF-19, expressed in the fetal brain. *Biochim Biophys Acta* 1444:148–151.
15. Nishimura T, Nakatake Y, Konishi M, Itoh N (2000) Identification of a novel FGF, FGF-21, preferentially expressed in the liver. *Biochim Biophys Acta* 1492:203–206.
16. Kharitonenkov A, et al. (2005) FGF-21 as a novel metabolic regulator. *J Clin Invest* 115: 1627–1635.
17. Ogawa Y, et al. (2007) BetaKlotho is required for metabolic activity of fibroblast growth factor 21. *Proc Natl Acad Sci USA* 104:7432–7437.
18. Kurosu H, et al. (2007) Tissue-specific expression of betaKlotho and fibroblast growth factor (FGF) receptor isoforms determines metabolic activity of FGF19 and FGF21. *J Biol Chem* 282:26687–26695.
19. Wu X, et al. (2007) Co-receptor requirements for fibroblast growth factor-19 signaling. *J Biol Chem* 282:29069–29072.
20. Suzuki M, et al. (2008) betaKlotho is required for fibroblast growth factor (FGF) 21 signaling through FGF receptor (FGFR) 1c and FGFR3c. *Mol Endocrinol* 22:1006–1014.
21. Kharitonenkov A, et al. (2008) FGF-21/FGF-21 receptor interaction and activation is determined by betaKlotho. *J Cell Physiol* 215:1–7.
22. Lin BC, Wang M, Blackmore C, Desnoyers LR (2007) Liver-specific activities of FGF19 require Klotho beta. *J Biol Chem* 282:27277–27284.
23. Hotta Y, et al. (2009) Fibroblast growth factor 21 regulates lipolysis in white adipose tissue but is not required for ketogenesis and triglyceride clearance in liver. *Endocrinology* 150:4625–4633.
24. Potthoff MJ, et al. (2009) FGF21 induces PGC-1alpha and regulates carbohydrate and fatty acid metabolism during the adaptive starvation response. *Proc Natl Acad Sci USA* 106:10853–10858.
25. Shimada T, et al. (2004) Targeted ablation of Fgf23 demonstrates an essential physiological role of FGF23 in phosphate and vitamin D metabolism. *J Clin Invest* 113: 561–568.
26. Powers CJ, McLeskey SW, Wellstein A (2000) Fibroblast growth factors, their receptors and signaling. *Endocr Relat Cancer* 7:165–197.
27. Yu C, et al. (2000) Elevated cholesterol metabolism and bile acid synthesis in mice lacking membrane tyrosine kinase receptor FGFR4. *J Biol Chem* 275:15482–15489.
28. Berglund ED, et al. (2009) Fibroblast growth factor 21 controls glycemia via regulation of hepatic glucose flux and insulin sensitivity. *Endocrinology* 150:4084–4093.
29. Xu J, et al. (2009) Fibroblast growth factor 21 reverses hepatic steatosis, increases energy expenditure, and improves insulin sensitivity in diet-induced obese mice. *Diabetes* 58:250–259.
30. Kurosu H, et al. (2006) Regulation of fibroblast growth factor-23 signaling by klotho. *J Biol Chem* 281:6120–6123.
31. Kolek OI, et al. (2005) 1alpha,25-Dihydroxyvitamin D3 upregulates FGF23 gene expression in bone: The final link in a renal-gastrointestinal-skeletal axis that controls phosphate transport. *Am J Physiol Gastrointest Liver Physiol* 289:G1036–G1042.
32. Inagaki T, et al. (2007) Endocrine regulation of the fasting response by PPARalpha-mediated induction of fibroblast growth factor 21. *Cell Metab* 5:415–425.
33. Badman MK, et al. (2007) Hepatic fibroblast growth factor 21 is regulated by PPARalpha and is a key mediator of hepatic lipid metabolism in ketotic states. *Cell Metab* 5:426–437.

Exp. Anim. 60(1), 57–63, 2011

—Original—

Kyoto Rhino Rats Derived by ENU Mutagenesis Undergo Congenital Hair Loss and Exhibit Focal Glomerulosclerosis

Takashi KURAMOTO[1)], Mitsuru KUWAMURA[2)], Fumi TAGAMI[1)], Tomoji MASHIMO[1)], Masato NOSE[3)], and Tadao SERIKAWA[1)]

[1)]Institute of Laboratory Animals, Graduate School of Medicine, Kyoto University, Sakyo-ku, Kyoto 606-8501, [2)]Laboratory of Veterinary Pathology, Osaka Prefecture University, Izumisano, Osaka 598-8531, and [3)]Department of Pathogenomics, Graduate School of Medicine, Ehime University, Toon, Ehime 791-0295, Japan

Abstract: *N*-ethyl-*N*-nitrosourea (ENU) mutagenesis is an important tool for studying gene function and establishing human disease models. Here, we report the characterization of a novel hairless mutant rat strain that carries a recessive mutation called Kyoto rhino (*krh*), which was created by ENU-mutagenesis. We produced a F344-*krh* strain through inbreeding without backcrossing to F344 rats. The *krh*/*krh* rats lost their coat hair by eight weeks of age. They also developed wrinkled skin, cystic hair canals and long curved nails by four months of age. Markedly dilated hair follicles that contained keratin debris were observed during histological analysis of the skin. The *krh* locus was mapped near the hairless (*Hr*) gene on chromosome 15. Sequence analysis revealed a nonsense mutation (c. 1238 C>A, p. S413X) in the *Hr* gene. The truncated HR protein was deduced to lack a zinc-finger domain and repression domains. In aged Hr^{krh}/Hr^{krh} rats, focal glomerulosclerosis (FGS) was observed in which collapsed glomeruli contained protein exudates in Bowman's capsule. Mesangial matrices that had proliferated in segments and foot processes that were fused in podocytes were also observed. The Hr^{krh}/Hr^{krh} rats also suffered from significant proteinuria. Given its breeding history, the F344-Hr^{krh} strain may harbor ENU-induced mutation(s) that underlie FGS in addition to having the Hr^{krh} mutation. The F344-Hr^{krh} rat is a useful model of skin disease and may provide a new model system for the examination of the pathogenesis of FGS.

Key words: disease model, hairless, mutation, nephrosis

Introduction

Hairless mutant rodents are valuable models for studying molecular mechanisms that underlie hair growth control. They are particularly valuable when searching for the genetic basis of hereditary human hair disorders.

In mice, 43 mutations are responsible for primary genetic hairlessness [7]. Among them, the most important are allelic mutations of the hairless (*Hr*) gene. The best characterized allele is the hairless (*hr*). Hr^{hr}/Hr^{hr} mice have a striking total alopecia phenotype which appears between three and four weeks of age. The pheno-

(Received 17 August 2010 / Accepted 16 September 2010)

Address corresponding: T. Kuramoto, Institute of Laboratory Animals, Graduate School of Medicine, Kyoto University, Yoshidakonoe-cho, Sakyo-ku, Kyoto 606-8501, Japan

type originates in the periorbital region and propagates in a wave-like fashion in the rostral-to-caudal direction [20]. It has been determined, through comparative studies of several distinct mouse *Hr* mutations, that the *Hr* gene product plays a key role in controlling hair follicle transformation during the catagen phase [20]. The hairless phenotype of *Hr*-mutant mice (Hr^{hr}/Hr^{hr}) is similar to that of the human disease atrichia. The disease phenotype comprises papular lesions (APL) and alopecia universalis congenital (ALUNC), complete hair loss after birth. It is a result of human *HR* mutation [2, 4, 9].

Another important mutant *Hr* of the mouse is the rhino (*rh*) mouse. Hr^{rh}/Hr^{rh} mice lose all of their hair by seven weeks of age, possess wrinkled skin and their nails overgrow. Additionally, they develop an autoimmune disease characterized by hypergammaglobulinemia, immunoglobulin deposits in the basement membrane of skin, spleen, liver, and kidney, and the presence of antinuclear antibodies which appear in young mice and increase with age [14].

Several rat hair loss mutations have been described. They are for the Charles River hairless rat [1], the Iffa Credo (IC) rat [6], the Hairless Wistar Yagi rat also known as the HWY/Slc rat [13], the Dundee experimental bald rat also known as the DEBR rat [22], the Bald rat [12], and the Hirosaki hairless rat (HHR) [17]. An intragenic deletion in the desmoglein 4 gene underlies the IC rat skin phenotype [6]. The absence of 80-kb of genomic DNA that contains five basic keratin genes is the cause of the HHR rat hairless phenotype [17].

Rat hair follicles are larger than those of mice. Therefore hairless mutant rats are attractive models for studying hair follicle development, differentiation, and cycling. Rat mutants are also good models for evaluating the effects of new drugs for treating human skin diseases. Therefore, it would be beneficial to establish new hairless rat models for these purposes.

We recently treated rats with *N*-ethyl-*N*-nitrosourea (ENU) to obtain different mutants [16]. Several hair loss phenotypes were identified by employing phenotype-driven screening. A hair loss mutant line was established by crossing mutant-type males with wild-type female littermates. Our analysis of the breeding record of this line can be used to prove that the hair loss phenotype is autosomal recessive. Thus, the mutation was named Kyoto rhino (*krh*).

In this study, we identified the *krh* mutation using a positional candidate approach and characterized the *krh/krh* rats. *krh* is a nonsense mutation of the rat *Hr* gene. *krh/krh* rats develop renal failure with massive proteinuria and focal glomerulosclerosis (FGS).

Materials and Methods

Animals

ENU-treated F344/NSlc male rats were mated with F344/NSlc female rats to generate G_1 offspring [16]. The ENU-mutagenized G_1 rats (n=42) were used as founders for the phenotype-driven screening of recessive mutations. Briefly, the G_1 rats were crossed with two F344 rats to generate G_2 offspring. The female G_2 offspring were then backcrossed with their parental G_1 rats to generate G_3 offspring. The recessive mutations induced by ENU in the G_1 rats become homozygous in the G_3 rats. Among the G_3 offspring (n=11) from a G_1 male (#E2307), three rats showed a hair loss phenotype; these rats were probands (P generation). We mated the affected rats with the normal littermates to fix the hair loss phenotype. The phenotype was fixed at the F_2 generation and the mutation was called *krh*. A mutant line was established by employing brother-sister mating (homozygous male × heterozygous female). The generation of inbreeding had reached F_6 at the end of August, 2010. The animal care and experimental procedures that were used were approved by the Animal Research Committee, Kyoto University and were carried out according to the Regulation on Animal Experimentation at Kyoto University.

Genetic mapping

Twenty N_2 rats were produced from a (BN/SsNSlc × F344-*krh/krh*)F_1 × F344-*krh/krh* backcross. The genotypes for the *krh* locus were identified on the basis of coat phenotype at four to five weeks of age. Genomic DNA was prepared from tail biopsies using an automatic DNA purification system (PI-200, Kurabo, Japan) and genotypes for *D15Rat10*, *D15Rat13*, and *D15Rat85* were determined. Linkage relationship was evaluated using the chi-square test of the Excel statistical package.

Confidence intervals ($P<0.05$) were calculated according to the method of a previous report [11].

RT-PCR and direct sequencing

Total RNA was isolated from the skin of five-week-old animals using ISOGEN (NIPPON GENE, Tokyo, Japan). RT-PCR and direct sequencing of the PCR product was carried out as described previously [15]. Rat *Hr* cDNA was amplified using the following eight primer sets: rHr-01&02 CACCTGTGGAAGGCTGCT and ACAGGGTCACTCTTGGGATG; rHr-03&04 AGGGACTACGCTGGAAGGAA and CCCAAACGTTACCGAGAGTG; rHr-05&06 GCAGGCAGCAGAATCTTTG and TCCTGTGGATGTCTCTGGTG; rHr-07&08 ACTCAAGAGGGCAGGCAGT and GGTGTTGAAGAGTCCGTGGT; rHr-09&10 CTTCCATCAACAAGGGCCTA and CTGGGCTCTCTGTGGAGTCT; rHr-11&12 GGTCAGCAGAAGGAACCAAC and TTCCAGAATGCTGTGCTGTC; rHr-13&14 GACTTAGCCTGTGGGGAATG and CTCCAAGGTTCCTGCTCCAG; rHr-15&16 GTCTCCAGGTAGCCAGACCA and GTTCCCTGCTTGTACCCAAA. The PCR products overlapped each other and spanned the entire 3,624 bp *Hr* coding sequence (CDS).

Morphological analysis

Dorsal and ventral skin samples were collected from *krh/krh* and *krh/+* littermates at two, nine and seventeen weeks of age. Mouse anti-cytokeratin (AE1/AE3, Dako Japan, Tokyo, Japan) was used for immunohistochemical analysis of the skin samples. Bound antibody was detected using horseradish peroxidase conjugated anti-mouse antibody (Histofine Simplestain MAX-PO; Nichirei, Tokyo, Japan) and 3,3'-diaminobenzidine as a chromogen (Vector Laboratories, Burlingame, CA, USA). To detect lipids, frozen sections were made from specimens that had been fixed with formalin and they were stained with Oil red O.

Organ samples of the heart, lungs, liver, pancreas, kidneys, spleen, lymph nodes, salivary glands, lacrimal glands, thyroid gland, adrenal glands, small and large intestines, and knee and foot joints, were collected from three *krh/krh* rats and three F344 rats at 40 weeks of age. They were fixed using 10% neutral buffered formalin, embedded in paraffin, cut at 4 μm in thickness, and then stained with hematoxylin and eosin (HE). To study glomerular lesions, periodic acid-Schiff (PAS) or periodic acid-methenamine-silver (PAM) staining was employed. For immunofluorescence studies, kidney samples were frozen in 22-oxacalcitriol compound (Miles Inc., Elkhart, IN, USA).

Electron microscopy

Perfusion fixation through the left ventricle was conducted with 4% paraformaldehyde in 0.1 M phosphate buffer (PB). Kidneys that had been excised were stored in 2% paraformaldehyde and 2.5% glutaraldehyde in 0.1 M PB. They were fixed with 2% osmic acid for 2 h and embedded in epoxy resin. Ultra-thin sections were double-stained with uranyl acetate and lead citrate and examined using a Hitachi H-7500 electron microscope (Hitachi, Tokyo, Japan).

Urine protein measurement

To collect urine, six male *krh/krh* rats and six F344/NSlc (+/+) rats, 40 weeks of age, were caged individually in metabolic chambers after they had been orally loaded with physiological saline at 2.5 ml/100 g body weight. Six-hour urine samples were collected and their volumes, and protein concentrations were determined. Statistical differences were determined using the Mann-Whitney U test.

Results

krh/krh rat hair loss phenotype and skin morphology

For the *krh/krh* rats, hair loss first occurred around the nose around 2 weeks after birth and extended gradually from the anterior to the posterior of the body (Fig. 1A and 1B). At around four months of age they had wrinkled skin, cystic hair canals and long curved nails.

Through histopathological analysis, markedly dilated hair follicles were observed. These cystic follicles contained a lot of keratin debris (Fig. 1C), and they stained positive for cytokeratin (Fig. 1D). The cysts were lined by a thin layer of squamous epithelium and an easily identifiable granular cell layer. The sebaceous glands that surrounded the dilated cysts were hyperplastic. Staining with Oil red O revealed that a large amount of lipids was present in the lumen of each cyst and on the

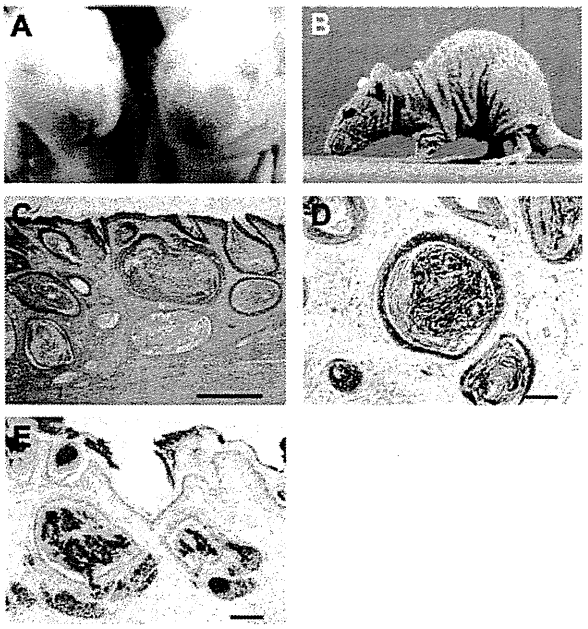

Fig. 1. Phenotypic and morphological characteristics of the Kyoto rhino rat. A: Right; a 2-week-old *krh/krh* rat with characteristic hair loss on the snout. Left; a littermate *krh/+* rat. B: Rhinocerotic appearance of a 10-week-old *krh/krh* rat. C: Histopathology of 9-week-old *krh/krh* rat skin. HE staining. Bar=500 μm. D: IHC of keratin of a 9-week-old *krh/krh* rat. Bar=100 μm. E: Oil Red O staining of a 17-week-old *krh/krh* rat. Bar=100 μm.

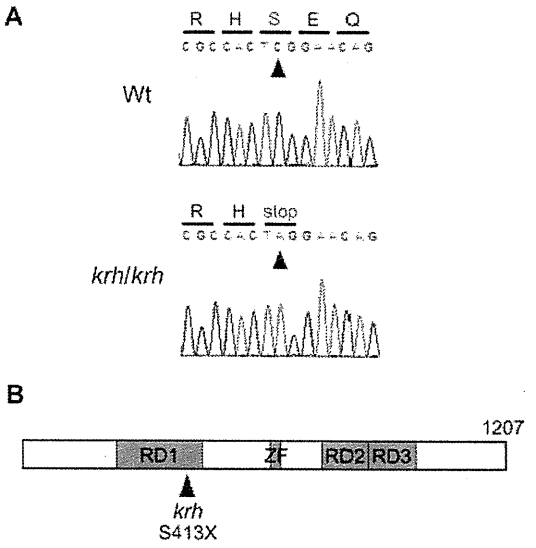

Fig. 2. Identification of the *krh* mutation. A: Results of direct sequencing of *Hr* cDNA of wild-type and *krh/krh* rats. The C-to-A nonsense mutation at position 1,238 is indicated by red arrowheads. The substitution produces a stop codon at amino acid residue 413 of protein HR. B: Schematic of the conserved domains in rat protein HR. RD1, RD2, and RD3 are used to denote the repression domains and ZF is used to denote the zinc-finger domain. The mutation site Ser413Ter is noted with a red arrowhead.

surface of the epidermis (Fig. 1E). These findings are indicators that the *krh/krh* skin and hair phenotypes are similar to those of *rh* at the *Hr* locus of the laboratory mouse [7].

krh is an Hr nonsense mutation

Hr on Chr 15 was believed to be the best candidate for *krh* and therefore the genotype of the backcross progeny was determined using genetic markers for Chr 15. We obtained 12 *krh/krh* and 8 *krh/+* rats from the (BN/SsNSlc × F344-*krh/krh*)F_1 × F344-*krh/krh* backcross. A significant linkage relationship was observed between *krh* and *D15Rat10* (42.7 Mb) with no recombination (χ^2=21.6, P<0.01), which is indicative that *krh* is located <13.9 cM away from *D15Rat10* with 95% probability [11]. *krh* was expected to span from 28.8 Mb to 56.6 Mb of Chr 15, within which the *Hr* locus (50.9 Mb) was mapped (RGSC v3.4).

Sequencing analyses of *Hr* cDNA obtained from *krh/krh* skin samples revealed that adenine (A) had been substituted for cytosine (C) at nucleotide position 1,238 from the start of the CDS (c. 1,238 C>A). This substitution resulted in a stop codon at amino acid 413 of the HR protein (p. Ser413Ter) (Fig. 2A). The truncated HR protein lacked a zinc-finger domain, a part of repression domain (RD) 1, and all of RD2 and RD3 (Fig. 2B). We characterized *krh* as an *Hr* nonsense mutation and called it Hr^{krh}.

Focal glomerulosclerosis and proteinuria in the aged Hr^{krh}/Hr^{krh} rat

Histopathological examinations of organs that were taken from Hr^{krh}/Hr^{krh} rats at 40 weeks of age were performed. No lesions that are associated with autoimmune diseases were observed, however, prominent glomerular lesions were noted in the kidneys of the Hr^{krh}/Hr^{krh} rats. These lesions were focal lesions that had collapsed glomeruli and protein exudates in Bowman capsule and the renal tubules (Fig. 3A and 3C), and segmental prolifera-

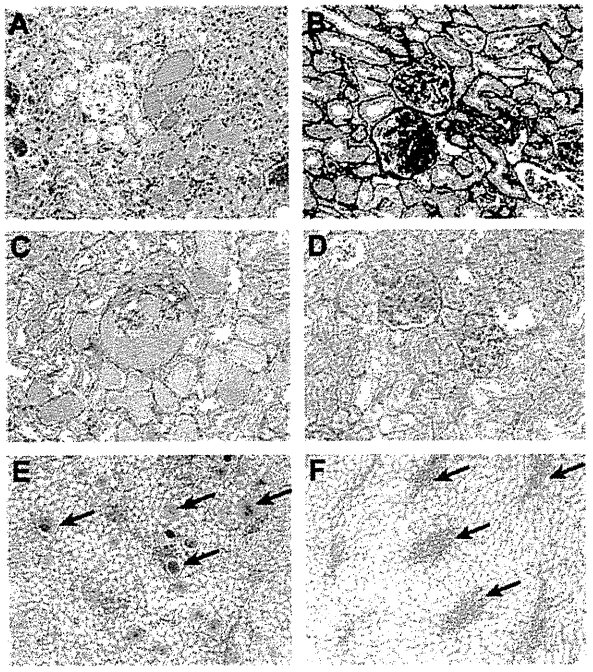

Fig. 3. Focal glomerular sclerotic lesions in 40-week-old Hr^{krh}/Hr^{krh} rat. Note that a collapsed glomerulus with protein exudates in Bowman's capsule and protein casts in renal tubules (A, C), and segmental proliferation of mesangial matrices (B, D) were seen. In the renal medulla, protein casts were notable in the collecting tubules (E) (arrows), but those in a wild-type F344 rat (+/+) were limited only to Henle's loop (F) (arrows). A: HE; B: PAM; C–F: PAS staining.

tion of the mesangial matrices (Fig. 3B and 3D). There was no inflammatory cell infiltration into the glomeruli and interstitium. In the renal medulla, protein casts were notably present in the collecting tubules (Fig. 3E). For the wild-type rats, protein casts were only observed in Henle's loop, possibly due to the effects of aging (Fig. 3F). These findings are indicators that the lesions that were observed in the F344-Hr^{krh}/Hr^{krh} rat were caused by focal glomerulosclerosis (FGS). Moreover, Hr^{krh}/Hr^{krh} rats at 40 weeks of age had proteinuria. The Hr^{krh} homozygous rats had significantly higher urine protein concentrations than age-matched wild-type rats: 152 ± 80.3 vs. 51.0 ± 38.5 mg/dl, (average ± SD), $P<0.02$ (Fig. 4).

From the electron microscopic observations, the segmental glomerular sclerotic lesions were characterized as having proliferating mesangial matrices (Fig. 5A). The proliferation was associated with the dendritic pro-

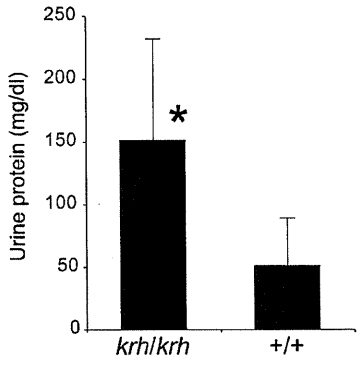

Fig. 4. Urine protein concentrations of Hr^{krh}/Hr^{krh} rats and wild-type F344 (+/+) rats. The Hr^{krh} homozygous rats had significantly higher urine protein concentrations than age-matched wild-type rats. Bars indicate standard deviation. *: $P<0.02$.

cesses of mesangial cells and on rare occasions with dense deposits in the mesangial regions. Foot process fusion was often observed in these glomeruli (Fig. 5B).

Discussion

The *krh* mutation was identified as an *Hr* nonsense mutation and therefore called Hr^{krh}. Protein HR is a nuclear receptor co-repressor for multiple nuclear receptors, such as the thyroid hormone receptor and the vitamin D receptor [23]. In the hair follicle (HF), the absence of functioning HR proteins results in the synthesis of premature and dysregulated catagen. This results in the destruction of the normal HF architecture and abrogates the HF's ability to cycle [20]. The Hr^{krh}/Hr^{krh} rat has cystic hair follicles and suffers from a premature hair cycle (Fig. 1). The truncated HR protein that is encoded by the Hr^{krh} nonsense mutation is caused by a lack of functional domains which play important roles in regulating target genes [23]. Additionally, the mutation may cause nonsense mediated mRNA decay. Therefore, it is likely that Hr^{krh} may be a loss-of-function mutation. In humans, *HR* mutations are associated with congenital alopecia, such as ALUNC and APL [2, 4, 9]. Because rats are suitably sized for handling and manipulating [5, 21], the Hr^{krh}/Hr^{krh} rat may be a useful animal model for developing therapies for these human diseases.

The aged Hr^{krh} homozygous rat has FGS which is as-

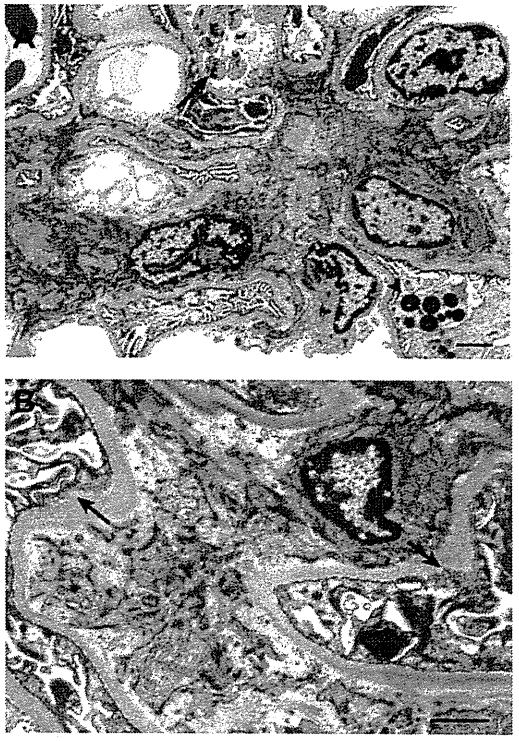

Fig. 5. Fine structures of glomerular lesions in the Hr^{krh}/Hr^{krh} rat. A: Proliferative lesions of mesangial matrices associated with significant dendritic projections from mesangial cells. Platelet aggregation was observed in a capillary loop (arrow). Intracellular hyaline droplets were significant in a podocyte (arrowhead). B: Foot process fusion (arrows) and a proliferative lesion of mesangial matrices that was not associated with dense deposits in mesangial regions and the glomerular basement membrane. Bar: 2 μm.

sociated with severe proteinuria. FGS is a descriptor for a pathological finding in the kidneys. When a nephritic range of proteinuria is observed, patients are diagnosed as having focal segmental glomerulosclerosis (FSGS). FSGS is classified by morphological variants including collapsed glomeruli, cellular proliferation, tip lesions, and diffuse mesangial proliferation [10]. The lesions that were observed in the F344-Hr^{krh} rat are characteristic of collapsed glomeruli associated with protein exudates in Bowman's capsule and may involve a collapsed variant of FSGS. Thus, the F344-Hr^{krh} rat may have potential as a model of nephritic FSGS.

FGS has not been reported for the APL or ALUNC family, and *Hr*-mutant mice, [2, 3, 7]. It is believed that FGS has a heterogeneous etiology and that it may manifest through multiple genetic factors [10]. The F344-Hr^{krh} rats were derived by employing ENU mutagenesis. The founder animals (G_1 generation) were expected to carry no more than four ENU-induced mutations in their CDS, if the CDS occupies 1% of the genome [16]. The F344-Hr^{krh} rats were mated by inbreeding without backcrossing to F344 rats to eliminate ENU-induced mutations other than the Hr^{krh} mutation. Thus, it is likely that the F344-Hr^{krh} rat may harbor mutation(s) that may play a role in the pathogenesis of FGS. FGS in Hr^{krh}/Hr^{krh} rats might be caused by unidentified mutation(s) that were induced by ENU or the combined effects of such mutation(s) with the Hr^{krh} mutation.

The Hr^{rh}/Hr^{rh} mouse has the nonsense mutation (R597X) [8] and develops hypergammaglobulinemia. The excess immunoglobulins that are produced due to this disease are deposited in the basement membranes of the skin, spleen, liver, and kidney, and antinuclear antibodies are produced. These symptoms appear in young mice and increase in severity with age [14]. Although the F344-Hr^{krh}/Hr^{krh} rat has a nonsense mutation (S413X), the mutation is not associated with an autoimmune disease or IgM, IgG, and C3 deposition in the kidneys (data not shown). Generally, pathological phenotypes that are associated with this disease are often influenced by a predisposed genetic background [18, 19]. Therefore, genes that are predisposed to causing autoimmune diseases in *rh/rh* mice may be absent in F344-Hr^{krh} rats. By replacing the genetic background of F344-Hr^{krh} with those of other rat strains, we might find autoimmune disease in Hr^{krh}/Hr^{krh} rats.

In summary, a novel rat mutant strain, F344-Hr^{krh}, was established that carries an *Hr* nonsense mutation (S413X). In addition to the hair loss phenotype, Hr^{krh} homozygous rats suffer from proteinuria and FGS. Therefore, F344-Hr^{krh} may have potential as a model of skin disease as well as nephritic FSGS.

Acknowledgments

This work was supported in part by Grants-in-aid for Scientific Research from the Japan Society for the Promotion of Science (21300153 to TK) and a Grant-in-aid for Cancer Research from the Ministry of Health, Labour

and Welfare. We are grateful to M. Yokoe, M. Terada, N. Takahira, and M. Sudo for their excellent technical assistance. Rat strain F344-*Hr*^{krh} (NBRP Rat No: 0471) is deposited in the National BioResource Project-Rat.

References

1. Ahearn, K., Akkouris, G., Berry, P.R., Chrissluis, R.R., Crooks, I.M., Dull, A.K., Grable, S., Jeruzal, J., Lanza, J., Lavoie, C., Maloney, R.A., Pitruzzello, M., Sharma, R., Stoklasek, T.A., Tweeddale, J., and King, T.R. 2002. The Charles River "hairless" rat mutation maps to chromosome 1: allelic with fuzzy and a likely orthologue of mouse frizzy. *J. Hered.* 93: 210–213.
2. Ahmad, W., Faiyaz ul Haque, M., Brancolini, V., Tsou, H.C., ul Haque, S., Lam, H., Aita, V.M., Owen, J., deBlaquiere, M., Frank, J., Cserhalmi-Friedman, P.B., Leask, A., McGrath, J.A., Peacocke, M., Ahmad, M., Ott, J., and Christiano, A.M. 1998. Alopecia universalis associated with a mutation in the human hairless gene. *Science* 279: 720–724.
3. Ahmad, W., Ratterree, M.S., Panteleyev, A.A., Aita, V.M., Sundberg, J.P., and Christiano, A.M. 2002. Atrichia with papular lesions resulting from mutations in the rhesus macaque (*Macaca mulatta*) hairless gene. *Lab. Anim.* 36: 61–67.
4. Ahmad, W., Zlotogorski, A., Panteleyev, A.A., Lam, H., Ahmad, M., ul Haque, M.F., Abdallah, H.M., Dragan, L., and Christiano, A.M. 1999. Genomic organization of the human hairless gene (*HR*) and identification of a mutation underlying congenital atrichia in an Arab Palestinian family. *Genomics* 56: 141–148.
5. Aitman, T.J., Critser, J.K., Cuppen, E., Dominiczak, A., Fernandez-Suarez, X.M., Flint, J., Gauguier, D., Geurts, A.M., Gould, M., Harris, P.C., Holmdahl, R., Hubner, N., Izsvak, Z., Jacob, H.J., Kuramoto, T., Kwitek, A.E., Marrone, A., Mashimo, T., Moreno, C., Mullins, J., Mullins, L., Olsson, T., Pravenec, M., Riley, L., Saar, K., Serikawa, T., Shull, J.D., Szpirer, C., Twigger, S.N., Voigt, B., and Worley, K. 2008. Progress and prospects in rat genetics: a community view. *Nat. Genet.* 40: 516–522.
6. Bazzi, H., Kljuic, A., Christiano, A.M., and Panteleyev, A.A. 2004. Intragenic deletion in the Desmoglein 4 gene underlies the skin phenotype in the Iffa Credo "hairless" rat. *Differentiation* 72: 450–464.
7. Bult, C.J., Eppig, J.T., Kadin, J.A., Richardson, J.E., and Blake, J.A. 2008. The Mouse Genome Database (MGD): mouse biology and model systems. *Nucleic Acids Res.* 36: D724–728.
8. Cachon-Gonzalez, M.B., San-Jose, I., Cano, A., Vega, J.A., Garcia, N., Freeman, T., Schimmang, T., and Stoye, J.P. 1999. The hairless gene of the mouse: relationship of phenotypic effects with expression profile and genotype. *Dev. Dyn.* 216: 113–126.
9. Cichon, S., Anker, M., Vogt, I.R., Rohleder, H., Putzstuck, M., Hillmer, A., Farooq, S.A., Al-Dhafri, K.S., Ahmad, M., Haque, S., Rietschel, M., Propping, P., Kruse, R., and Nothen, M.M. 1998. Cloning, genomic organization, alternative transcripts and mutational analysis of the gene responsible for autosomal recessive universal congenital alopecia. *Hum. Mol. Genet.* 7: 1671–1679.
10. Dagati, V. 1994. The many masks of focal segmental glomerulosclerosis. *Kid. Int.* 46: 1223–1241.
11. Friedman, J.M., Leibel, R.L., and Bahary, N. 1991. Molecular mapping of obesity genes. *Mamm. Genome* 1: 130–144.
12. Inazu, M. and Sakaguchi, T. 1984. Morphologic characteristics of the skin of bald mutant rats. *Lab. Anim. Sci.* 34: 584–587.
13. Ishii, Y., Tsutsui, S., Doi, K., and Itagaki, S. 1997. Hair follicles of young Wistar strain hairless rats: a histological study. *J. Anat.* 191: 99–106.
14. Kawaji, H., Tsukuda, R., and Nakaguchi, T. 1980. Immunopathology of rhino mouse, an autosomal recessive mutant with murine lupus-like disease. *Acta Pathol. Jpn.* 30: 515–530.
15. Kuramoto, T., Kitada, K., Inui, T., Sasaki, Y., Ito, K., Hase, T., Kawagachi, S., Ogawa, Y., Nakao, K., Barsh, G.S., Nagao, M., Ushijima, T., and Serikawa, T. 2001. Attractin/mahogany/zitter plays a critical role in myelination of the central nervous system. *Proc. Natl. Acad. Sci. U.S.A.* 98: 559–564.
16. Mashimo, T., Yanagihara, K., Tokuda, S., Voigt, B., Takizawa, A., Nakajima, R., Kato, M., Hirabayashi, M., Kuramoto, T., and Serikawa, T. 2008. An ENU-induced mutant archive for gene targeting in rats. *Nat. Genet.* 40: 514–515.
17. Nanashima, N., Akita, M., Yamada, T., Shimizu, T., Nakano, H., Fan, Y., and Tsuchida, S. 2008. The hairless phenotype of the Hirosaki hairless rat is due to the deletion of an 80-kb genomic DNA containing five basic keratin genes. *J. Biol. Chem.* 283: 16868–16875.
18. Nose, M. 2007. A proposal concept of a polygene network in systemic vasculitis: lessons from MRL mouse models. *Allergol. Int.* 56: 79–86.
19. Nose, M., Nishimura, M., and Kyogoku, M. 1989. Analysis of granulomatous arteritis in MRL/Mp autoimmune disease mice bearing lymphoproliferative genes. The use of mouse genetics to dissociate the development of arteritis and glomerulonephritis. *Am. J. Pathol.* 135: 271–280.
20. Panteleyev, A.A., Botchkareva, N.V., Sundberg, J.P., Christiano, A.M., and Paus, R. 1999. The role of the hairless (*hr*) gene in the regulation of hair follicle catagen transformation. *Am. J. Pathol.* 155: 159–171.
21. Serikawa, T., Mashimo, T., Takizawa, A., Okajima, R., Maedomari, N., Kumafuji, K., Takami, F., Neoda, Y., Otsuki, M., Nakanishi, S., Yamasaki, K., Voigt, B., and Kuramoto, T. 2009. National BioResource Project-Rat and related activities. *Exp. Anim.* 58: 333–341.
22. Sun, J., Silva, K.A., McElwee, K.J., King, L.E., and Sundberg, J.P. 2008. The C3H/HeJ mouse and DEBR rat models for alopecia areata: review of preclinical drug screening approaches and results. *Exp. Dermatol.* 17: 793–805.
23. Thompson, C.C., Sisk, J.M., and Beaudoin, G.M. 3rd. 2006. Hairless and Wnt signaling: allies in epithelial stem cell differentiation. *Cell Cycle* 5: 1913–1917.

Neurobiology of Disease 41 (2011) 261–269

Contents lists available at ScienceDirect

Neurobiology of Disease

journal homepage: www.elsevier.com/locate/ynbdi

Scn1a missense mutation causes limbic hyperexcitability and vulnerability to experimental febrile seizures

Yukihiro Ohno [a,*], Shizuka Ishihara [a], Tomoji Mashimo [b], Nobumasa Sofue [a], Saki Shimizu [a], Takuji Imaoku [a], Toshiko Tsurumi [b], Masashi Sasa [c], Tadao Serikawa [b]

[a] *Laboratory of Pharmacology, Osaka University of Pharmaceutical Sciences, Osaka 569-1094, Japan*
[b] *Institute of Laboratory Animals, Graduate School of Medicine, Kyoto University, Kyoto 606-8501, Japan*
[c] *Nagisa Clinic, Osaka 573-1183, Japan*

ARTICLE INFO

Article history:
Received 17 May 2010
Revised 15 August 2010
Accepted 19 September 2010
Available online 25 September 2010

Keywords:
Febrile seizure
$Na_v1.1$ channel
Scn1a
Missense mutation
Rat model

ABSTRACT

Mutations of the voltage-gated sodium (Na_v) channel subunit SCN1A have been implicated in the pathogenesis of human febrile seizures including generalized epilepsy with febrile seizures plus (GEFS+) and severe myoclonic epilepsy in infancy (SMEI). Hyperthermia-induced seizure-susceptible (Hiss) rats are the novel rat model carrying a missense mutation (N1417H) of Scn1a, which is located in the third pore-forming region of the $Na_v1.1$ channel. Here, we conducted behavioral and neurochemical studies to clarify the functional relevance of the Scn1a mutation *in vivo* and the mechanism underlying the vulnerability to hyperthermic seizures. Hiss rats showed markedly high susceptibility to hyperthermic seizures (mainly generalized clonic seizures) which were synchronously associated with paroxysmal epileptiform discharges. Immunohistochemical analysis of brain Fos expression revealed that hyperthermic seizures induced a widespread elevation of Fos-immunoreactivity in the cerebral cortices including the motor area, piriform, and insular cortex. In the subcortical regions, hyperthermic seizures enhanced Fos expression region—specifically in the limbic and paralimbic regions (e.g., hippocampus, amygdala, and perirhinal–entorhinal cortex) without affecting other brain regions (e.g., basal ganglia, diencephalon, and lower brainstem), suggesting a primary involvement of limbic system in the induction of hyperthermic seizures. In addition, Hiss rats showed a significantly lower threshold than the control animals in inducing epileptiform discharges in response to local stimulation of the hippocampus (hippocampal afterdischarges). Furthermore, hyperthermic seizures in Hiss rats were significantly alleviated by the antiepileptic drugs, diazepam and sodium valproate, while phenytoin or ethosuximide were ineffective. The present findings support the notion that Hiss rats are useful as a novel rat model of febrile seizures and suggest that hyperexcitability of limbic neurons associated with Scn1a missense mutation plays a crucial role in the pathogenesis of febrile seizures.

Introduction

Febrile seizures (FS) are the most common type of seizures in childhood, often occurring between 6 months and 5 years of age. Although most FS are generally benign, one-third are complex and exhibit persistent and/or recurrent seizures (Fetveit, 2008; Scantlebury and Heida, 2010; Shinnar, 2003). Specifically, patients of generalized epilepsy with febrile seizures plus (GEFS+) exhibit FS in childhood progressing to generalized epilepsy in adults and, in some cases, accompany variable symptoms including tonic–clonic, absence, and/or myoclonic seizures (Scheffer and Berkovic, 1997). Severe myoclonic epilepsy in infancy (SMEI) is more severe usually beginning within the first 6 months after birth, followed by progressive worsening of seizures associated with ataxia and mental decline (Dravet et al., 2005; Incorpora, 2009). Although familial or twin studies have shown that genetic predisposition contributes to the etiology of FS (Baulac et al., 2004; Baulac and Baulac, 2009; Nakayama, 2009), the causative genes and pathogenic mechanisms underlying human FS are still elusive.

Voltage-gated sodium (Na_v) channels mediate the generation and propagation of action potentials in electrically excitable cells such as neurons and muscles. They are classified into 9 subtypes encompassing $Na_v1.1$ to $Na_v1.9$ and have a common structure composed of 4 homologous domains, each of which contains voltage-sensor and pore-forming regions. Among these subtypes, $Na_v1.1$ channels have been implicated in the pathogenesis of multiple types of FS (Meisler and Kearney, 2005; Ragsdale, 2008). Specifically, more than 200 mutations in human $Na_v1.1$ channel α subunit SCN1A have been reported in patients with FS

Abbreviations: ACF, artificial cerebrospinal fluid; FS, febrile seizure; GEFS+, generalized epilepsy with febrile seizures plus; Na_v, voltage-gated sodium; PBS, phosphate-buffered saline; IR, immunoreactivity; SMEI, severe myoclonic epilepsy in infancy.

* Corresponding author. Fax: +81 72 690 1053.
E-mail address: yohno@gly.oups.ac.jp (Y. Ohno).

Available online on ScienceDirect (www.sciencedirect.com).

0969-9961/$ – see front matter © 2010 Elsevier Inc. All rights reserved.
doi:10.1016/j.nbd.2010.09.013

including GEFS+ and SMEI (Meisler and Kearney, 2005; Ragsdale, 2008). The 13 SCN1A mutations found in patients with GEFS+ are known to be missense mutations, while about half of the SMEI mutations are missense and the remaining are truncated mutations (e.g., nonsense or frame-shift mutations) (Meisler and Kearney, 2005; Mulley et al., 2005). In addition, recent studies have shown that haploinsufficiency of $Na_v1.1$ channel causes hypersusceptibility to hyperthermic seizures and sporadic spontaneous seizure in mice, which accompanied a marked reduction in sodium currents in inhibitory GABAergic neurons (Yu et al., 2006; Oakley et al., 2009; Martin et al., 2010). All these findings indicate a close relationship between the $Na_v1.1$ channel function and the etiology of FS. Nonetheless, due to the diversity of functional changes of $Na_v1.1$ channels in patients with FS (Meisler and Kearney, 2005; Catterall et al., 2010), the precise mechanism and functional relevance of the SCN1A mutations underlying the pathogenesis of FS remain to be clarified.

Using the gene-driven *N*-ethyl-*N*-nitrosourea mutagenesis, we have recently generated a rat model which carries a missense mutation (N1417H) in the third pore-forming region of Scn1a (Mashimo et al., 2010). We designated them hyperthermia-induced seizure-susceptible (Hiss) rats because of their high susceptibility to hyperthermia-induced seizures. Since missense mutations in the pore-forming region of $Na_v1.1$ channels are frequently reported in patients with SMEI or GEFS+ (Meisler and Kearney, 2005; also see Fig. 1), Hiss rats may serve as a useful FS model with a genetic background similar to that of SMEI or GEFS+. Indeed, the mutation site in Hiss rats is very close to one (V1428A) of the GEFS+ mutations (Sugawara et al., 2001). In our previous studies (Mashimo et al., 2010), Hiss rats at a very young age (1–5 weeks old) exhibited a high susceptibility to hyperthermia-induced seizures. Electrophysiological analysis of the N1417H mutant channels or hippocampal neurons dissociated from Hiss rats revealed that N1417H mutation causes a hyperpolarized shift in the voltage dependency of $Na_v1.1$ channel inactivation and a slight increase in persistent leak current. In addition, hippocampal bipolar neurons (i.e., GABAergic interneurons) exhibited a significant decrease in spike amplitude, indicating reduced function of $Na_v1.1$ channels. These changes in $Na_v1.1$ functions were specifically observed in the biplolar neurons but not in the pyramidal neurons (Mashimo et al., 2010). Thus, our findings suggest that the Scn1a missense mutation impairs functions of the hippocampal GABAergic neurons to confer FS susceptibility. Nonetheless, the functional relevance of the Scn1a missense mutation *in vivo* and its mechanism underlying the vulnerability of animals to hyperthermic seizures remain to be determined.

In the present study, therefore, we further conducted behavioral and neurochemical studies to clarify pathophysiological mechanisms underlying the seizure vulnerability in Hiss rats. In addition, responses of hyperthermic seizures in Hiss rats to antiepileptic drugs were also evaluated to assess their clinical relevance as a human FS model. The present results show that the N1417H mutation of Scn1a markedly enhances the excitability of the corticolimbic neural circuit and the limbic vulnerability to hyperthermic seizures. Hiss rats seem to be a useful rat model for understanding the etiology of FS and also for searching new drugs to treat FS.

Materials and methods

Animals

Hiss rats (F344-*Scn1a*$^{Kyo811/Kyo811}$) were obtained from the National BioResource Project for the Rat (NBRPR#0455) in Japan. As reported previously (Mashimo et al., 2010), Hiss rats carry homozygous

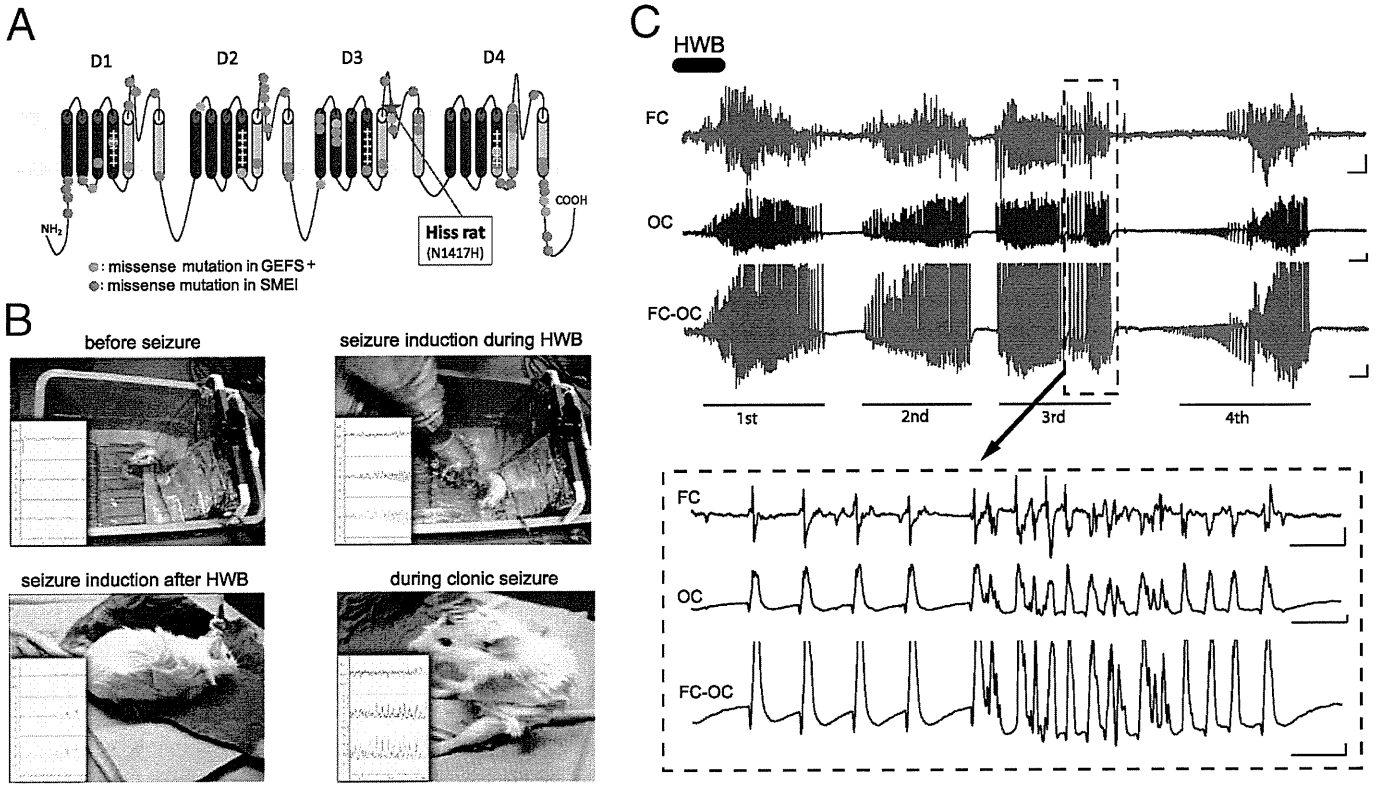

Fig. 1. Hyperthermic seizures and EEG in Hiss rats. (A) Structure of Scn1a and location of the missense mutation N1417H in Hiss rats. Scn1a consists of 4 homologous domains (D1–D4), each of which contains voltage-sensor and pore-forming regions. As a reference, missense mutation sites reported in GEFS+ and SMEI are also shown (Meisler and Kearney, 2005). (B) Photos illustrating induction of hyperthermic seizures and simultaneously monitored EEG in Hiss rats. Hiss rats were immerged in a hot water bath (HWB: 45 °C) for a maximum of 5 min or until a seizure occurred. Cortical EEG was simultaneously monitored under freely-moving conditions. All Hiss rats mainly developed clonic seizures (barely tonic–clonic seizures), which usually repeated even after HWB. (C) Typical paroxysmal discharges in Hiss rats. Solid lines (1st–4th) under EEG chart indicate the period of clonic seizures. Calibration: upper panel, 100 μV and 2 sec; lower panel, 100 μV and 1 sec.

Scn1a$^{Kyo81/Kyo8111}$ alleles, where *Scn1a* gene has a missense mutation N1417H in the third pore-forming region of $Na_v1.1$ channels (Fig. 1). Hiss rats were backcrossed more than 5 generations against F344/NSlc inbred background to eliminate mutations in chromosomal regions other than the *Scn1a* locus. F344/NSlc (F344) rats were used as control animals. The animals were kept and bred at the Institute of Laboratory of Animals, Graduate School of Medicine, Kyoto University in air-conditioned rooms (24 ± 2 °C and 50% ± 10% relative humidity) under a 14-h light/10-h dark cycle (lights on: 7:00 a.m.). The housing conditions and the animal care methods complied with the Guidelines for Animal Experiments of Kyoto University. The experimental protocols of this study were also approved by the Experimental Animal Research Committee at Osaka University of Pharmaceutical Sciences.

Hyperthermic seizure induction and EEG recording

Male juvenile Hiss or F344 rats (4 weeks old) were used. To implant EEG recording electrodes, animals were anesthetized with pentobarbital (40 mg/kg, i.p.) and fixed in a stereotaxic instrument (David Kopf Instruments, CA, USA). Small holes were made in the skull, and silver ball electrodes were placed on the surface of the right or left frontal and occipital cortex. A reference electrode was placed on the frontal cranium. The electrodes were then connected to a miniature plug and fixed to the skull with dental cement. After a 1-week recovery period, animals with chronically implanted electrodes were subjected to the following experiments.

Hyperthermic seizures were evoked by immersing the animals in a hot water bath as published previously (Mashimo et al., 2010). Briefly, the animals were placed in a temperature-controlled water bath (30 cm × 60 cm × 60 cm) containing about 15 cm depth 45 °C water for a maximum of 5 min or until a seizure occurred. Under freely moving conditions, cortical EEG was recorded simultaneously with behavioral observation using an amplifier (MEG-6108; Nihon Kohden) and a thermal alley recorder (RTA-1100; Nihon Kohden, Tokyo, Japan). The recorded signals were stored in a computer (PowerLab ML845; AD Instruments Japan, Nagoya, Japan) for later analysis.

Forebrain Fos expression following hyperthermic seizures

Male juvenile Hiss or F344 rats (4 weeks old) were subjected to the hyperthermic seizure experiments in the same manner as described previously. Two hours after the hyperthermic seizure or the end (5 min) of bathing, the animals were deeply anesthetized with pentobarbital (80 mg/kg, i.p.), transcardially perfused with ice-cold phosphate-buffered saline (PBS) and then with 4% formaldehyde solution. The brains were removed from the skull and placed in fresh fixative for at least 24 hours. After postfixation, coronal sections (30 μm thickness) were cut from each brain using a Microslicer (DSK-3000, Dosaka, Kyoto Japan).

The staining of Fos-immunoreactivity (IR) was performed by a method published previously (Ohno et al., 2009). Briefly, slices were washed with PBS containing 0.3% Triton X-100, and incubated for 2 hours in the presence of 2% normal rabbit serum, and then again in the presence of 2% normal rabbit serum and goat c-Fos antiserum (Santa Cruz Biotechnology Inc., Santa Cruz, CA) for an additional 18–36 hours. After washing with PBS, the sections were incubated with a biotinylated rabbit anti-goat IgG secondary antibody (Vector Laboratories, Burlingame, CA) for 2 hours. The sections were then incubated with PBS containing 0.3% hydrogen peroxide for 30 min to inactivate the endogenous peroxidase. Thereafter, the sections were washed with PBS and incubated for 2 hours with avidin–biotinylated horseradish peroxidase complex (Vectastain ABC Kit). Fos-IR was visualized by the diaminobenzidine–nickel staining method.

Fos expression was quantified by counting the number of Fos-IR-positive nuclei in the following regions (Paxinos and Watson, 2007): 1) the cerebral cortices = the medial prefrontal cortex (mPFC), motor cortex (MC), sensory cortex (SC), agranular insular cortex (AIC), piriform cortex (Pir), auditory cortex (AuC); 2) the limbic/paralimbic areas = CA1, CA3, and dentate gyrus (DG) of the hippocampus, basomedial amygdaloid nucleus (BMA), perirhinal–entorhinal cortex (PRh–Ent), cingulated cortex (CgC), lateral septal nucleus (LS), core (AcC), and shell (AcS) parts of the nucleus accumbens; 3) the basal ganglia = dorsolateral (dlST) and dorsomedial (dmST) striatum and globus pallidus (GP); 4) the diencephalon = paratenial (PT), anteromedial (AM), centromedial (CM) and ventromedial (VM) thalamus, lateral habenula (LHb), anterior (AH), posterior (PH), and dorsomedial (DMH) hypothalamus; 5) the lower brainstem = locus coeruleus (LC), central gray (CG), pontine reticular nucleus (PnR), gigantocellular reticular nucleus (GiR), and inferior olivary nucleus (IO). The number of Fos-IR-positive nuclei was counted within a 350 × 350 μm^2 grid laid over each of the above brain regions by observers who were blinded regarding the seizure incidence.

Hippocampal afterdischarges

Male Hiss or F344 rats (8–10 weeks old) were used. Under pentobarbital (40 mg/kg, i.p.) anesthesia, animals were chronically implanted with electrodes as described previously. Namely, a silver ball electrode was placed on the surface of the right frontal cortex and a stainless-steel bipolar electrode was inserted to the ipsilateral hippocampus (P: 3.8, L: 2.0, H: −2.2 mm from the cortical surface) for EEG recording. A bipolar stimulation electrode was also inserted to a position 0.5 mm anterior to the recording site for local stimulation of the hippocampus. All electrodes including a reference electrode were then connected to a miniature plug and fixed to the skull.

After a 1-week recovery period, animals were subjected to the assessment of the stimulus threshold for hippocampal afterdischarges. Briefly, hippocampal and cortical EEG were recorded under freely moving conditions. Local stimulation consisting of square pulses (duration: 100 μsec, frequency: 20 Hz) was then applied to the hippocampus for 5 sec with increasing intensity by 25 μA a step, and the stimulus threshold for induction of the hippocampal afterdischarges was measured.

Evaluation of the effects of antiepileptic drugs

Juvenile Hiss rats of either sex (4 weeks old) were used. Animals were given either antiepileptic drug as follows; diazepam (0.5 and 1 mg/kg, i.p.), sodium valproate (100–300 mg/kg, i.p.), ethosuximide (100 mg/kg, i.p.) and phenytoin (20 and 40 mg/kg, i.p.). Thirty minutes after the drug treatment, animals were subjected to the hyperthermic seizure experiments as described previously. The number of seizure incidences, total duration of seizures (i.e., sum of the duration of each seizure), and latency for the first seizure induction were compared with those of the control values with the vehicle alone. In a separate series of experiments, the effects of antiepileptics on the body (rectal) temperature of Hiss rats were also examined. For these studies, animals were given the above doses of the antiepileptic drugs and, 30 min later, the rectal temperature was measured.

Drugs

The drugs used in this study were as follows: sodium valproate, ethosuximide and phenytoin (Sigma-Aldrich), and diazepam (Cercine®, Takeda Pharmaceuticals Co., Ltd., Osaka, Japan). Diazepam, sodium valproate, and ethosuximide were dissolved and/or diluted with physiological saline. Phenytoin was first dissolved in a small amount of 0.5 N NaOH and then diluted with saline. The

Vectastain ABC kit and DAB substrate were purchased from Vector Laboratories (CA, USA). All other reagents were obtained from commercial sources.

Statistical analysis

Data are expressed as the mean ± SEM. The statistical significance of differences in the number of Fos-IR-positive cells, the threshold level of hippocampal afterdischarges, the number and latency of spike generation in the hippocampal CA1 neurons, and the effects of antiepileptic drugs between two groups (Hiss and F344 rats) was determined by the Student's *t*-test. Comparisons of the parameters among multiple groups were analyzed by one-way ANOVA and Tukey's *post-hoc* multiple comparison test.

Results

Hyperthermic seizures in Hiss rats

We have previously demonstrated that Hiss rats show much higher susceptibility than F344 rats to seizures induced by stimulation of hot water (45 °C) bathing, with a significantly lower body (rectal) temperature (Mashimo et al., 2010). In this study, we measured EEG epileptiform discharges during hyperthermic seizures and quantified the latency for seizure induction, number of seizures, duration of each seizure and total duration of all seizures. Juvenile Hiss or F344 rats, which were chronically implanted with EEG electrodes, were placed in a 45 °C hot water bath for 5 min (Fig. 1). Under these conditions, none of F344 rats exhibited any seizures or abnormal behaviors during 5 min of bathing. However, all Hiss rats ($N=5$) examined

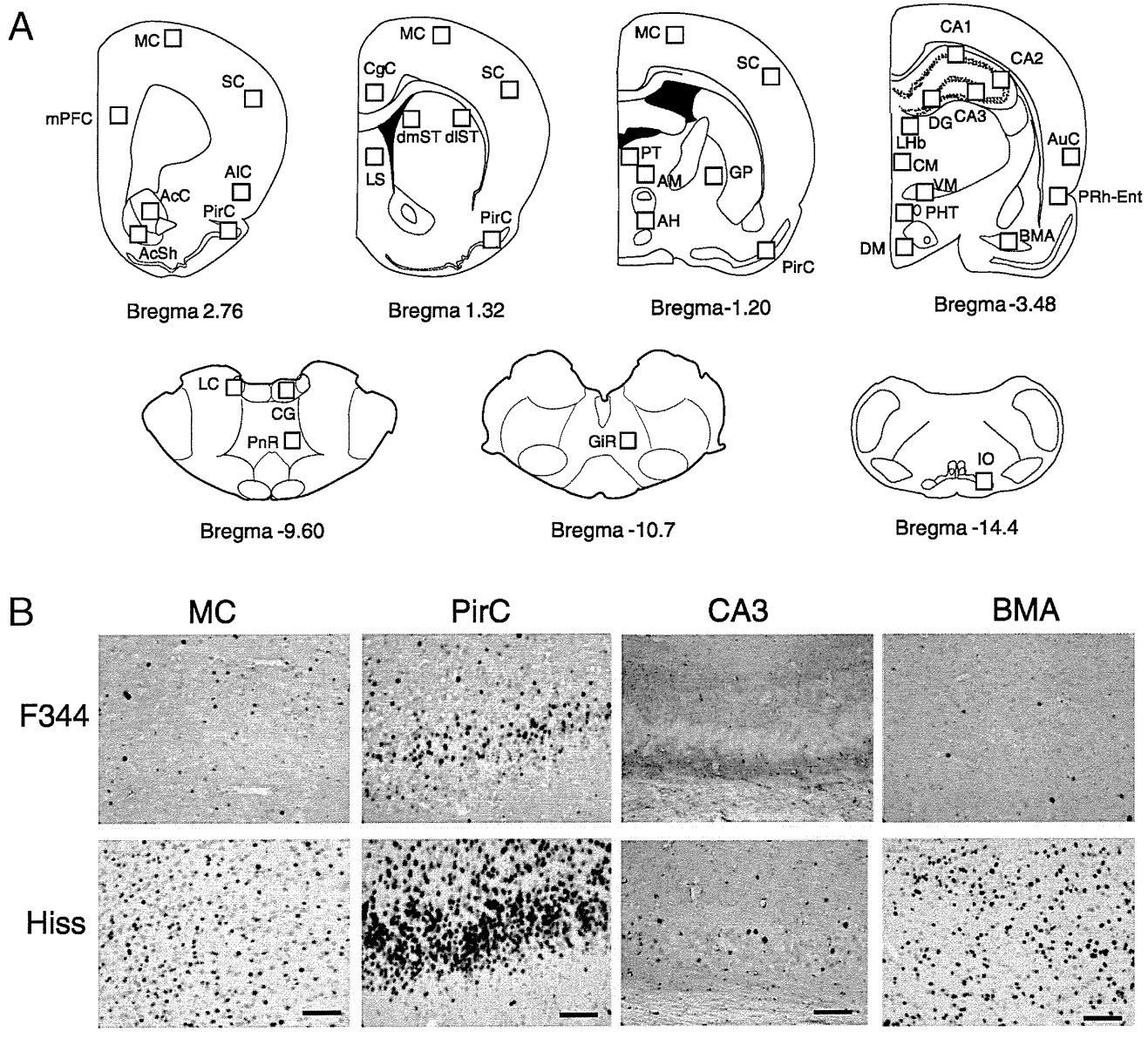

Fig. 2. Fos expression analysis following hyperthermic seizures. (A) Schematic illustrations of the brain sections selected for quantitative analysis of Fos-IR-positive cells. An anteroposterior coordinate (distance from the bregma) is shown on the bottom of each brain section. Open squares in each section indicate the sample areas analyzed; mPFC: the medial prefrontal cortex, MC: motor cortex, SC: sensory cortex, AIC: agranular insular cortex, PirC: piriform cortex, AcC and AcS: core and shell regions of the nucleus accumbens, respectively, CgC: cingulated cortex, LS: lateral septum, dlST and dmST: dorsolateral and dorsomedial striatum, respectively, GP: globus pallidus, PT, AM, CM, and VM: paratenial, anteromedial, centromedial, and ventromedial thalamus, respectively, LHb: lateral habenula, AH, PH, and DMH: anterior, posterior and dorsomedial hypothalamus, respectively, PRh–Ent: perirhinal–entorhinal cortex, AuC: auditory cortex, DG: dentate gyrus of the hippocampus, BMA: basomedial amygdaloid nucleus, LC: locus coeruleus, CG: central gray, PnR: pontine reticular nucleus, GiR: gigantocellular reticular nucleus, IO: inferior olivary nucleus. (B) Representative photographs illustrating the Fos-IR-positive cells in the MC, PirC, CA3 of the hippocampus and BMA in Hiss and F344 rats. Scale bar: 100 μm.

showed hyperthermic seizures with a mean latency of 201 ± 14.7 sec. Hyperthermic seizures in Hiss rats were mainly consisted of clonic convulsions of forelimbs and body trunk which occasionally extended to tonic–clonic convulsions (Fig. 1). In addition, hyperthermic seizures were completely synchronized with the incidence of paroxysmal epileptiform discharges in EEG, which mainly consisted of large multiple spikes, spike and wave discharges or fast waves (Fig. 1). The hyperthermic seizures in Hiss rats occurred repeatedly after removing the animals from the bath. The number of seizure incidence, duration of each seizure, and total seizure duration estimated by EEG discharges were 2.20 ± 0.48 times, 28.1 ± 4.70 sec, and 62.2 ± 16.1 sec, respectively ($N = 5$).

Hyperthermic seizure-induced Fos expression

Fos protein is widely used as a biological marker to map neural excitation in the brain in response to various stimuli such as convulsions, stress, pain, and various pharmacological manipulations (Morgan and Curran, 1989; Ohno et al., 2008; 2009). We analyzed forebrain Fos expression following hyperthermic seizures in Hiss rats in order to identify the brain regions responsible for the seizure generation.

As compared to the control animals (F344 rats) which showed no seizures with the hot water bathing, Hiss rats exhibited a marked increase in Fos expression in a various regions of the cerebral cortices such as the motor cortex, piriform cortex, agranular insular cortex, and medial prefrontal cortex following the hyperthermic seizures (Figs. 2 and 3). The elevation of Fos expression due to hyperthermic seizures in the cerebral cortex widely spread in the anteroposterior and mediolateral axis of both hemispheres, reflecting generalized seizure characteristics. In the subcortical regions, Hiss rats exhibited a marked elevation of Fos expression in the limbic and paralimbic structures, specifically in the amygdala (i.e., basomedial amygdala), hippocampus (i.e., dentate gyrus and CA3), and perirhinal–entorhinal

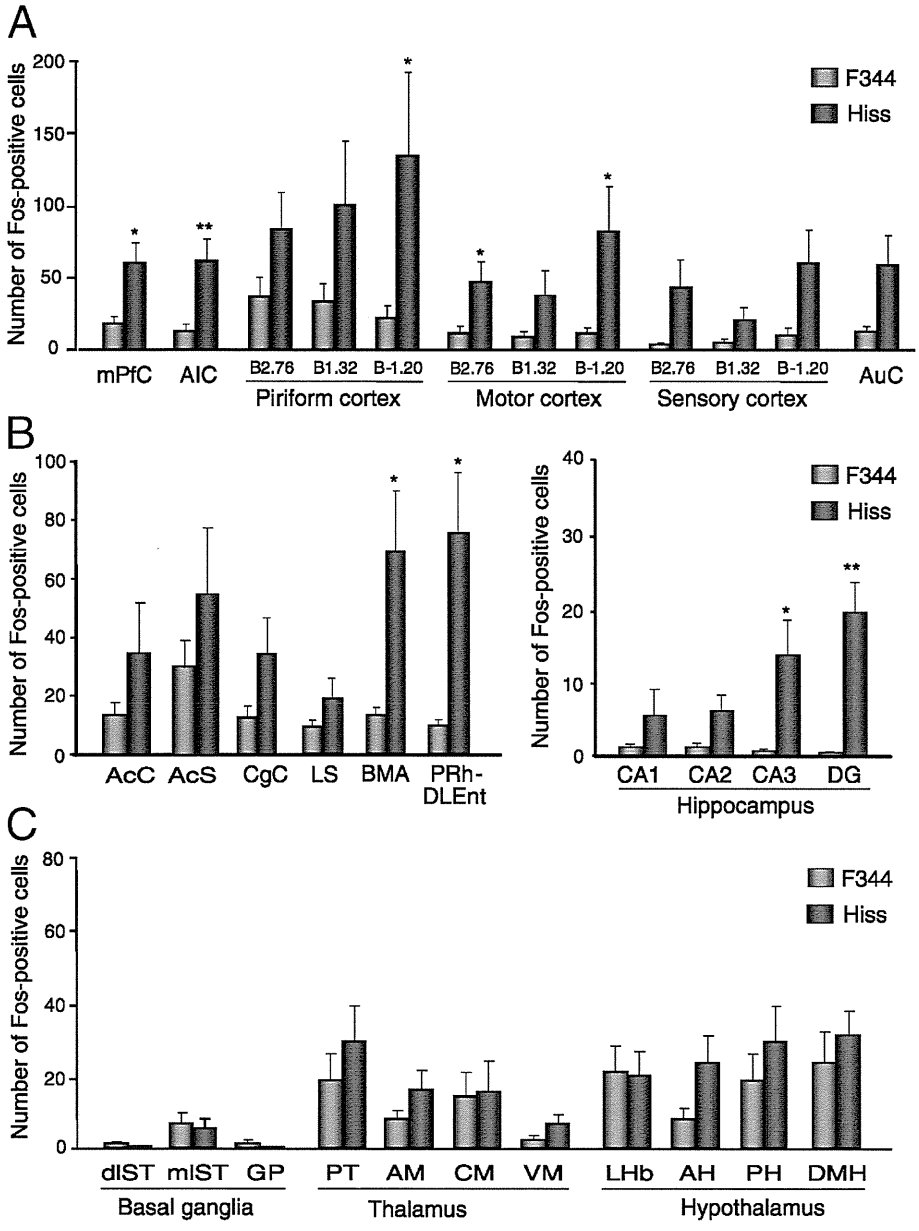

Fig. 3. Regional Fos expression induced by hyperthermic seizures in Hiss rats. The brain was removed 2 hours after the incidence of hyperthermic seizure (Hiss rats) or the end (5 min) of bathing (F344 rats). (A) Fos expression in the cerebral cortex. (B) Fos expression in the limbic and paralimbic regions. (C) Fos expression of the basal ganglia and brainstem regions. Abbreviations for the brain sample areas are the same as in Fig. 2. Each column represents the mean ± SEM. $^{*}P<0.05$, $^{**}P<0.01$; Significantly different from F344 (Control) rats.

cortex (Figs. 2 and 3). Although the changes did not reach statistical significance, Fos expression in the CA1 and CA2 fields also increased to about 5 times the control levels. In contrast to the limbic-paralimbic regions, Fos expression in the basal ganglia (e.g., striatum and globus pallidus) or diencephalon (e.g., thalamus and hypothalamus) were not significantly altered by the hyperthermic seizures (Figs. 2 and 3). In addition, both Hiss and control rats showed only negligible Fos expression in the lower brainstem structures including the locus coeruleus, pontine reticular nucleus, central gray, gigantocellular reticular nucleus, and inferior olivary nucleus (data not shown).

Changes in threshold of hippocampal afterdischarges

Since the limbic region including the hippocampus seemed to be the site of neural excitation responsible for the hyperthermic seizures in subcortical regions, we examined the susceptibility of Hiss rats to hippocampal afterdischarges upon local stimulation. Hiss or F344 rats were chronically implanted with EEG electrodes and the stimulus threshold for induction of the hippocampal afterdischarges was measured under freely moving conditions. As shown in Fig. 4, Hiss rats exhibited a significantly lower threshold than in the control animals in evoking the hippocampal afterdischarges. The duration of the hippocampal afterdischarges also tended to increase more in Hiss rats than in the control animals.

Effects of antiepileptic drugs on hyperthermic seizures

We evaluated the action of several antiepileptic drugs against the hyperthermia-induced seizures in Hiss rats. Hyperthermic seizures were evoked by the hot water bathing as described previously. The number of seizure incidences, the total duration of hyperthermic seizures, and the latency for seizure induction in Hiss rats were compared to those of the control (F344) rats which were given the vehicle alone. As shown in Fig. 5, the anticonvulsant diazepam (0.5 and 1 mg/kg, i.p.) significantly inhibited the incidence of hyperthermic seizures with significant prolongations in the seizure latency. Sodium valproate (100–300 mg/kg, i.p.) also dose-dependently inhibited the incidence of hyperthermic seizures (Fig. 5). In contrast, neither phenytoin nor ethosuximide inhibited hyperthermic seizures, although slight increases in the seizure latency were observed with both agents (Fig. 5).

In a separate series of experiments, we also examined the effects of the above antiepileptics on body (rectal) temperature in Hiss rats. Neither diazepam, valproate, nor ethosuximide at the highest dose examined showed any effects on the body temperature of Hiss rats (Table 1). However, phenytoin significantly lowered the body temperature in a dose-related fashion (Table 1).

Discussion

Previous studies have shown that a loss-of-function of Scn1a with truncated mutations causes a dysfunction of inhibitory GABAergic neurons, which consequently elicits hyperexcitability of the brain leading to seizures (Oakley et al., 2009; Ogiwara et al., 2007; Yu et al., 2006). Nonetheless, the functional relevance of the Scn1a missense mutations remains to be clarified due to the diversity of functional changes of the $Na_v1.1$ channels in FS patients (Meisler and Kearney, 2005; Catterall et al., 2010). Analysis using recombinant $Na_v1.1$ channels revealed that the Scn1a missense mutations cause a variety of effects on the channel functions such as either or mixed pattern of a gain-of-function (e.g., increased persistent leak current, depolarized shift in voltage dependence of inactivation, hyperpolarized shift in voltage dependence of activation) or a loss-of-function (e.g., hyperpolarized shift in voltage dependence of inactivation and depolarized shift in voltage-dependence of activation) changes (Cossette et al., 2003; Lossin et al., 2002; 2003; Meisler and Kearney, 2005; Rhodes et al., 2004; Spampanato et al., 2004; Tang et al., 2009). Although the phenotypic alterations associated with these mutations are not fully evaluated, we (Mashimo et al., 2010) and other group (Martin et al., 2010) recently demonstrated that the Scn1a missense mutation impairs the function of inhibitory GABAergic neurons and markedly enhances the incidence of hyperthermic seizures.

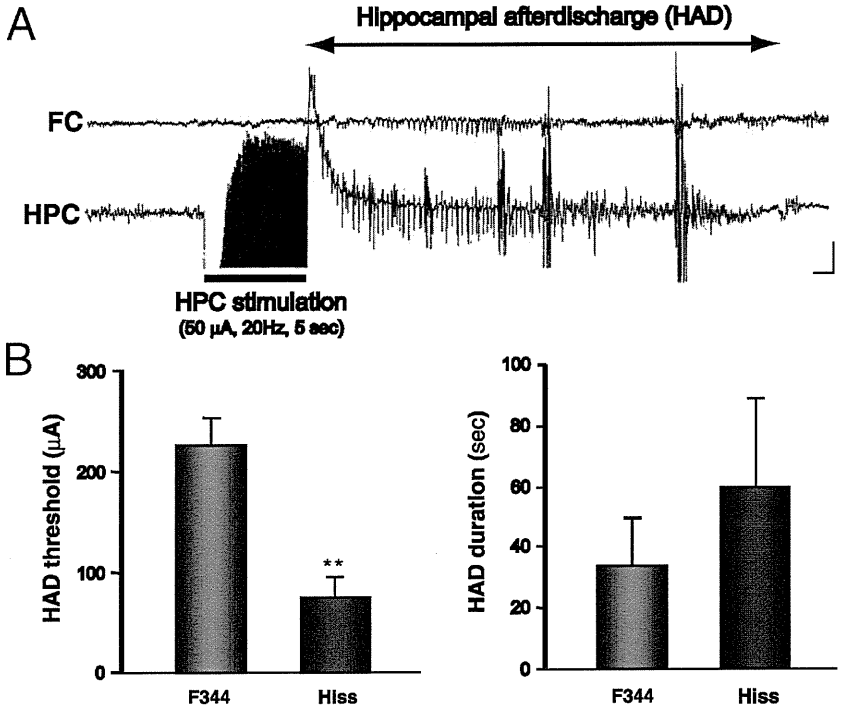

Fig. 4. Hippocampal afterdischarges in Hiss rats. Through a chronically implanted electrode, local stimulation (100 μsec, 20 Hz) was applied to the hippocampus for 5 sec with increasing the intensity by 25 μA per step, and the stimulus threshold for induction of the hippocampal afterdischarges (HAD) was measured. (A) Typical EEG chart illustrating HAD in Hiss rats. Calibration: 100 μV and 1 sec. (B) Stimulus threshold for the induction of HAD and HAD duration in Hiss and F344 rats. Each column represents the mean ± SEM. $^{**}P<0.01$; Significantly different from F344 (Control) rats.

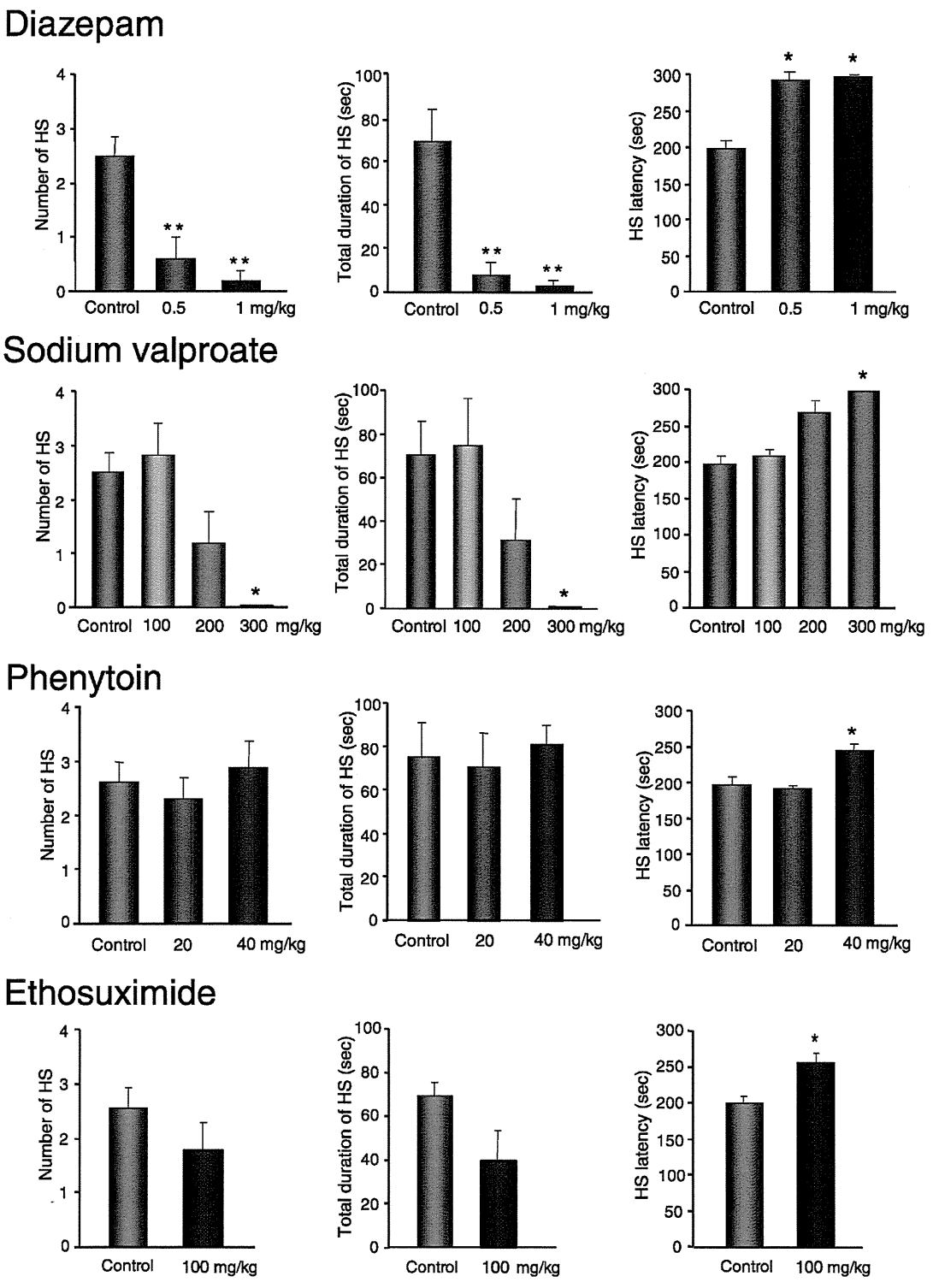

Fig. 5. Effects of antiepileptic drugs on hyperthermic seizures in Hiss rats. Animals were treated with either diazepam (0.5 and 1 mg/kg, i.p.), sodium valproate (100–300 mg/kg, i.p.), phenytoin (20 and 40 mg/kg, i.p.), or ethosuximide (100 mg/kg, i.p.) and 30 min later subjected to the hyperthermic seizure experiments. Each column represents the mean ± SEM. $^{*}P<0.05$, $^{**}P<0.01$; Significantly different from the Control values with vehicle alone.

In the present study, we confirmed and quantified the susceptibility of Hiss rats to hyperthermic seizures by simultaneously monitoring EEG and behaviors. Although the gross behaviors remain unaltered, Hiss rats exhibited repeated and reproducible convulsive seizures upon the hyperthermia stimulation, which were completely synchronized with paroxysmal epileptiform discharges. Immunohistochemical analysis of brain Fos expression illustrated that hyperthermic seizures in Hiss rats caused an extensive increase in Fos-IR in the cerebral cortices (e.g., motor, piriform, and insular cortex) probably reflecting the generalized features of hyperthermic seizures. Fos analysis also revealed that hyperthermic seizures in Hiss rats are closely associated with hyperexcitability of limbic neurons. Among various subcortical regions examined, Fos expression was region-specifically elevated in the limbic and paralimbic regions such as the